LUND UNIVERSITY

Model catalysts studied by x-rays, visible and infrared light

Albertin, Stefano

2021

Document Version:
Publisher's PDF, also known as Version of record

Link to publication

Citation for published version (APA):
Albertin, S. (2021). *Model catalysts studied by x-rays, visible and infrared light*. Lund.

Total number of authors:
1

LUND UNIVERSITY

PO Box 117
221 00 Lund
+46 46-222 00 00

Model catalysts studied by x-rays, visible and infrared light

By Stefano Albertin

DOCTORAL DISSERTATION

To be presented, with permission of the Faculty of Science, Lund University, for public criticism in the lecture Rydberg hall at the Department of Physics on Friday, the 10th of December 2021 at 09:15

Dissertation Advisors:
Prof. Edvin Lundgren, Dr. Uta Hejral, Dr. Johan Gustafson

Faculty Opponent:
Prof. Irene Groot
Leiden University, the Netherlands

Organization
LUND UNIVERSITY
Synchrotron Radiation Research
Department of Physics
Box 118
SE-221 00 Lund, Sweden

Document name
DOCTORAL DISSERTATION

Date of issue
10/12/2021

Sponsoring organization

Author(s)
Stefano Albertin

Title and subtitle
Model catalysts studied by x-rays, visible and infrared light

Abstract

This work is focused on the study of transition metal model catalysts for gas-phase heterogeneous catalysis, studied with light-based in-situ and operando techniques.

Metallic model catalysts, such as Palladium (Pd) and Iridium (Ir) single crystals and in minor part deposited Rhodium (Rh), were studied using a combination of x-ray and non x-ray techniques. The aim was to either acquire structural characterization of new materials or pushing the state-of-the-art instrumental boundaries and close the material and pressure gap present in model catalysts studies. In this context were developed new techniques, such as Transmission Surface Diffraction (TSD), or further refined and validated, such as 2D Surface Optical Reflectance (2D-SOR).

Pd, used in papers I,II , III , V , IX, was studied with a combination of X-ray Photoelectron Spectroscopy (XPS) and X-ray Diffraction (XRD) techniques as well as 2D-SOR and planar induced fluorescence (PLIF). This model catalyst was used as proof of concept for new approaches and new set-ups developed in collaboration with the combustion physics division, Lund University. One example is the use of the newly developed POLARIS High-Pressure XPS (HPXPS) station at P22 at PETRA III, Desy, Germany, demonstrating the potential and a new state-of-the-art of operando XPS. During this investigation, we have also confirmed Pd metallic islands' formation on PdO during reduction, a potentially critical factor in the modification and/or enhancement of the system catalytic activity. Another important result is obtained combining high energy surface X-ray Diffraction (HESXRD) with 2D-SOR and PLIF, and the characterization of 2D-SOR with an atomically precise diffraction method. During this investigation in particular we characterized the 2D-SOR sensitivity down to 2-3 Å by the observation of 2D-SOR signal from thin PdO $(\sqrt{5}x\sqrt{5})R27°$.

Similarly to Pd, in paper VI, we used Rh nanoparticles and films to implements a novel approach of Transmission Surface Diffraction (TSD) in which, at normal incidence angle, we performed diffraction in transmission through the sample with the use of high energy x-rays. With this contribution, we show that it is indeed possible to obtain reliable data in this configuration, contributing to mitigating the experimental challenges of experiments otherwise performed at grazing incidence geometry.

Ir, used in papers VII, IX, VIII, was studied with XPS and XRD techniques to further understand the behavior of this, previously less investigated, catalyst that has recently gained popularity in both gas-heterogeneous as well as electrocatalysis community. XPS results provide further information on Ir metal and Ir oxide's reactivity and thermal stability while XRD results show the complex behavior of the catalyst under oxidation and reduction conditions. In particular, during the reduction it was observed the formation of Ir metallic islands on to of IrO_2, in a parallel to the Pd/PdO/Pd case, and suggesting a possible general behavior for oxidized metal catalysts systems. The combination of these, both thermodynamic and structural data, provide new and much-needed information to the catalysis community, and at the same time, encourage a more well-defined approach to the IrO_2/Ir(100) system.

Key words: High Energy Surface X-ray Diffraction, X-ray Photoelectron Spectroscopy, Oxidation, Pd(100), PdO, Ir(100), IrO_2, In-situ, Operando, Surface Optical Reflectance

Classification system and/or index termes (if any):

Supplementary bibliographical information:

Language
English

ISSN and key title:

ISBN
978-91-8039-065-1 (print)
978-91-8039-066-8 (pdf)

Recipient's notes

Number of pages
267

Price

Security classification

Distribution by Stefano Albertin I, the undersigned, being the copyright owner of the abstract of the above-mentioned dissertation, hereby grant to all reference sources permission to publish and disseminate the abstract of the above-mentioned dissertation.

Signature_______________________________ Date 10/12/2021

DOKUMENTDATABLAD enl SIS 61 41 21

Model catalysts studied by x-rays, visible and infrared light

By Stefano Albertin

LUND
UNIVERSITY

Cover image: HESXRD 2D-detector image of IrO_2/Ir system, combined with impressionist painting via AI algorithm *Deep Dream Generator*

Funding information: This thesis work was financially supported by Knut and Alice Wallenberg Foundation (19651218-4018, Atomistic Design of Catalysts)

Faculty of Science, Department od Physics, Division of Synchrotron Radiation Research
ISBN: 978-91-8039-065-1 (print)
ISBN: 978-91-8039-066-8 (pdf)

Printed in Sweden by Media-Tryck, Lund University, Lund 2020

”Men wanted for hazardous journey.
Low wages, bitter cold, long hours of complete darkness.
Safe return doubtful.
Honour and recognition in event of success."
Recruitment flyer (apocryphal)
Imperial Trans-Antarctic Expedition (1914-1917)
Ernest H. Shackleton

Contents

Preface

List of Publications

This dissertation is based on the following publications:

I **Surface optical reflectance combined with x-ray techniques during gas-surface interactions**

S. Albertin, J. Gustafson, J. Zhou, S. Pfaff, M. Shipilin, S. Blomberg, L. R. Merte,.O Gutowski, A-C. Dippel, J. Zetterberg, E. Lundgren and U. Hejral

J. Phys. D: Appl. Phys. 2020, 53 224001

I performed much of the experimental work as well as the data analysis. I wrote a computed code that allowed to extract quantitative data from the experiments and wrote the paper.

II **CO oxidation under lean conditions over Pd(100)model catalyst studied by photoelectron spectroscopy at total pressure of 0.5 bar: closing the gap**

S. Albertin, C. Goodwin, M. Shipilin, P. Lömker, A. Nilsson, U. Hejral, S. Blomberg, C. Schlueter, and E.Lundgren

(Manuscript form)

I performed much of the experimental work as well as the data analysis. I wrote a computed code that allowed to extract quantitative data from the experiments and wrote the paper.

III **Combining high-energy x-ray diffraction with surface optical reflectance and planar laser induced fluorescence for operando catalyst surface characterization**

S. Pfaff, J. Zhou, U. Hejral, J. Gustafson, M. Shipilin, S. Albertin, S. Blomberg, O. Gutowski, A. Dippel, E. Lundgren, and J. Zetterberg

Rev. Sci. Instrum. 2019, 90, 033703

I performed much of the experimental work and was involved in the discussion about the paper.

IV **Bridging the pressure gap in CO oxidation**

S. Blomberg, U. Hejral, M. Shipilin, S. Albertin, H. Karlsson,C. Hulteberg, P. Lömker, C. Goodwin, D. Degerman, J. Gustafsson, C. Schlueter, A. Nilsson, E. Lundgren and P. Amann

ACS Catal. 2021, 11, 15, 91289135

I was involved in the measurements and discussion about the paper.

V **The structure of the active Pd state during catalytic CO oxidization**

C. M. Goodwin, M. Shipilin, S. Albertin, U. Hejral, P. Lömker, H. Wang, S. Blomberg, D. Degermann, C. Schlueter, A. Nilsson, E. Lundgren and P. Amann

J. Phys. Chem. Lett. 2021, 12, 18, 44614465

I performed much of the experimental work and was involved in the discussion about the paper.

VI **Transmission surface diffraction applied to model catalyst surfaces during catalytic gas-surface interactions**

U. Hejral, S. Albertin, S. Pfaff, T. Wiegmann, J. Drnec, O. Balmes, M. Shipilin, J. Zhou, O. Gutowski, J. Gustafson, and E. Lundgren

(Manuscript form)

I was involved in the design of part of the experimental the setup, I performed much of the experimental work and was involved in the discussion about the paper.

VII **The oxidation and reduction of Ir(100) studied by high energy surface x-ray diffraction**

S. Albertin, E. Lundgren, L. R. Merte, R. Martin, J. F. Weaver, A. Dippel, O. Gutowski, and U. Hejral

(Submitted to J. Phys. Chem. C.)

I performed much of the experimental work as well as the data analysis and wrote the paper.

VIII **High-resolution x-ray photoelectron spectroscopy of an $IrO_2(110)$ film on Ir(100)**

R. Martin, M. Kim, C. J. Lee, V. Mehar, S. Albertin, U. Hejral, L. R. Merte, E. Lundgren, A. Asthagiri, and J. F. Weaver

J. Phys. Chem. Lett. 2020, 11, 17, 71847189

I was involved in the measurements and discussion about the paper.

IX **Isothermal reduction of IrO_2 (110) films by methane investigated using in situ x-ray photoelectron spectroscopy**

R. Martin, M. Kim, C. J. Lee, V. Mehar, S. Albertin, U. Hejral, L. R. Merte, A. Asthagiri, and J. F. Weaver

ACS Catal. 2021, 11, 9, 5004-5016

I was involved in the measurements and discussion about the paper.

Related paper that are not included in this thesis:

X **Ammonia oxidation over a $Pt_{25}Rh_{75}(001)$ model catalyst surface: an operando study**

A. Resta, U. Hejral, S. Blomberg, S. Albertin, A. Vlad, Y. Garreau, C. Chatelier, F. Venturini, P. Ferrer, G. Held, D. Grinter, E. Lundgren, and A. Coati

J. Phys. Chem. C 2020, 124, 40, 2219222199

I was involved in the measurements and discussion about the paper

XI **Reduced CO saturation coverage on vicinal Pd surfaces: the importance of the adsorption site**

F. Garcia-Martinez, E. Dietze, F. Schiller, D. Gajdek, L. R. Merte, S. Gericke, J. Zetterberg, A. B. Preobrajenski, S. Albertin, E. Lundgren, H. Grönbeck, and J. E. Ortega

J. Phys. Chem. Lett. 2021, 12, 39, 9508-9515

I was involved in the measurements and discussion about the paper

List of Abbreviations

2D-SOR	2D Surface Optical Reflectance
APXPS	Ambient Pressure X-ray Photoelectron Spectroscopy
BCC	Body Centered Cubic
CTR	Crystal Truncation Rod
CUS	Coordinatively Unsaturated
DFT	Density Functional Theory
EM	Electro-Magnetic
FCC	Face Centered Cubic
GIXPS	Grazing Incidence X-ray Photoelectron Spectroscopy
HAXPES	Hard X-rays Photoelectron Spectroscopy
HCP	Hexagonal Close Packed
HESXRD	High Energy Surface X-Ray Diffraction
HPXPS	High Pressure X-ray Photoelectron Spectroscopy
HRCLS	High Resolution photoelectron Core-Level Specroscopy
IMFP	Inelastic Mean Free Path
MS	Mass Spectrometer
NPs	NanoParticles
PLIF	Planar Induced Fluorescence
PVD	Physical Vapor Deposition
QMS	Quadrupole Mass Spectrometer
SXRD	Surface X-Ray Diffraction
TSD	Transmission Surface Diffraction
UHV	Ultra High Vacuum

XPS	X-ray Photoelectron Spectroscopy
XRD	X-Ray Diffraction
XRR	X-Ray Reflectivity

Abstract

This work is focused on the study of transition metal model catalysts for gas-phase heterogeneous catalysis, studied with light-based *in-situ* and *operando* techniques.

Metallic model catalysts, such as Palladium (Pd) and Iridium (Ir) single crystals and in minor part deposited Rhodium (Rh), were studied using a combination of x-ray and non x-ray techniques. The aim was to either acquire structural characterization of new materials or pushing the state-of-the-art instrumental boundaries and close the material and pressure gap present in model catalysts studies. New techniques were developed in this context, such as Transmission Surface Diffraction (TSD), or further refined and validated, such as 2D Surface Optical Reflectance (2D-SOR).

Pd, used in **papers I,II , III , V, IX**, was studied with a combination of X-ray Photoelectron Spectroscopy (XPS) and X-ray Diffraction (XRD) techniques as well as 2D-SOR and planar induced fluorescence (PLIF). This model catalyst was used as proof of concept for new approaches and new set-ups developed in collaboration with the combustion physics division at Lund University. One example is the use of the newly developed POLARIS High-Pressure XPS (HPXPS) station at P22 at PETRA III, Desy, Germany, demonstrating the potential and a new state of the art of *operando* XPS. During this investigation, we have also confirmed Pd metallic islands' formation on PdO during reduction, a potentially critical factor in the modification and/or enhancement of the system catalytic activity. Another important result is obtained combining high energy surface X-ray Diffraction (HESXRD) with 2D-SOR and PLIF, and the characterization of 2D-SOR with an atomically precise diffraction method. During this investigation in particular we characterized the 2D-SOR sensitivity down to 2-3 Å by the observation of 2D-SOR signal from thin PdO $(\sqrt{5} \times \sqrt{5})$R27°.

Similarly to Pd, in **paper VI**, we used Rh nanoparticles and films to implement a novel approach of Transmission Surface Diffraction (TSD) in which, at normal incidence angle, we performed diffraction in transmission through the sample with the use of high energy x-rays. With this contribution, we show that it is indeed possible to obtain reliable information in this configuration, contributing to mitigating the experimental challenges of experiments otherwise performed at grazing incidence geometry.

Ir, used in **papers VII, VIII, IX**, was studied with XPS and XRD techniques to further understand the behavior of this, previously less investigated, catalyst that has recently gained popularity in both gas-heterogeneous as well as electro-catalysis community. XPS results provide further information on Ir metal and Ir oxide's reactivity and thermal stability while XRD results show the complex behavior of the catalyst under oxidation and reduction conditions. In

particular, during the reduction it was observed the formation of Ir metallic islands on to of IrO_2 phase, in a parallel to the Pd/PdO/Pd case, and suggesting a possible general behaviour for oxidized metal catalysts systems to form such layered structures. The combination of these, both thermodynamic and structural data, provide new and much-needed information to the catalysis community, and at the same time, encourage a more well-defined approach to the IrO_2/Ir(100) system.

Popular Science

Material science is nowadays responsible for our living standards and stands as a cornerstone of innumerable advances in industry and technology, which we increasingly rely upon for everyday life. One of the most prolific and industrious sub-category within material science is chemistry, and within chemistry, one of the if not the most, relevant classes of chemical reactions are *heterogeneous catalytic reactions.*

In this class of *reactions* the chemicals react on top - and thanks to - materials called *catalysts* that are in a *heterogeneous* phase [1] compared to the reactants. These catalysts, without being consumed by the chemical reaction, allow the process to proceed through a different *chemical pathway* compared to what would otherwise happen at the same reaction without them, enhancing the kinetics of the process.

Since the reactions happen at the interface and thanks to surfaces, a great emphasis has been put on studying them with atomic accuracy, using and developing new techniques in the field of *surface science.* This approach has the aim, once understood the nature of the catalytic process, to be able to tailor future catalysts for specific applications.

Since industrial chemical reactions usually happen in very complex and dangerous environments, a common approach in research is to simplify them, creating *model systems.* Using simplified materials, *model catalysts*, in low-pressure environment and simple chemical reactions. These systems, although they present a certain "gap" [2] between them and the real systems, are studied as close to real operation condition (called *operando*) and without exposing the system to environmental conditions that could affect the catalyst behaviour (*in-situ*).

In this work, it has been chosen to study, with spectroscopic and diffraction techniques, a handful of reactions and model catalysts to further the atomistic understanding of these during reaction conditions.

---

[1] the phase is the state of matter: solid, liquid or gas. A common example of heterogeneous catalysis could be, for instance, reacting gasses on top of a solid catalyst.

[2] This gap is generally referred to as *Material and Pressure Gap*

Acknowledgement

"Man is fond of counting his troubles but he does not count his joys.
If he counted them up, as he ought to,
he would see that every lot has enough happiness provided for it."
- Fyodor Dostoevsky -

Looking behind, it is clear that it has been a long, challenging, and fun ride. And I'm sure that it has not been for me alone, but for all the people I had the luck to meet and work with in these five years at the Division of Synchrotron Radiation (Research?...). To all of you, thank you.

I would like to name, even briefly, the important people that have shaped this time, in no particular order if not my own "flow of consciousness". Also, there will likely be a certain amount of superlatives: please bear with it, it's not for lack of imagination but only the vocabulary to describe superlative people.

First and foremost, I would like to mention my supervisors Uta Hejral, Edvin Lundgren, and Johan Gustafson. Unarguably my most heartfelt thanks goes to **Uta** with which I spent truly countless hours in labs and conferences all over the world. Working together has been amazingly fun, tiring and, no doubt, the most intensely instructive period of my life. To **Edvin** and **Johan** goes my gratitude for the guide, time revising an infinite number of drafts, and help to learn the rope of the job for what is important for synchrotron science and scientists. Bringing me all over the world, always with a smile and an anecdote, presenting my work and getting to know scientists all over.

Secondly, I would like to mention all those collaborators that, one way or another, have helped me understand and produce, but even a little, some science. **Lidsay Merte** that has been a massive help and an inexhaustible cornucopia of knowledge, no matter the field. **Andreas Schaefer** which I met only briefly, but which sense of humor and infinite love for science I still hold dear. My collaborators from Florida **Jason Waver** and **Rachel Martin**, which I spent some time on conference and beamtime. Both professor and student, burning for science and always up for a hop on the other side of the globe, document permitting...

Although maybe briefly met, I would like to sincerely thanks all the people I spent some lovely time doing science and eating candy, with **Mikhail Shipilin**, **Christopher M. Goodwin** and **Patrick Lömker** from P22/LTH. Fantastic conversationalists and remarkable scientists, always ready to teach me how to fix the beam, calculate some value or teach me about photography or getting to meet wives, if only by stories. **Andrea Resta**, scientist *extraordinaire*, with which I spent good times doing science, listening to music, and talking about motorcycle trips. **Roberto Felici** and **Olivier Balmes**, along with Edvin, two of the kindest and most knowledgeable people I met and I had the privilege to learn from.

Furthermore, and not in order of importance, I would like to thanks all the people at the division. The two "oldest", my officemate **Payam Shayesteh** and my *de-facto* officemate **Andrea Troian**. Countless coffees, a good deal of swearing, and a lot of science, thank you guys. **Alfred Larsson**, **Giuseppe Abbondanza**, **Giulio D'Acunto**, **Yen-Po Liu**, **Virginia Boix**, **Claudiu Bulbucan**, **Tamires Gallo**, **Weronica Linpe** and all the amazing people as SLJUS: when not at the office taking coffee and trying to help each other, a good company during barbecue, a trip or in front of a beer, wasting time and relaxing.

A spot of honor, at least to me, goes to one of the funniest, nicest and warmest people I could ever find, always up for "something" and permanently running around, even more than I, **Dorotea Gajdek**: thank you for endless discussion, beers and some of the most relaxing times I had.

My thanks also to all the people from Combustion Physics at Lund University, that for short or long, I shared beamline hutches with: **Johan Zetterberg**, **Sara Blomberg**, **Sebastian Pfaff**, **Sabrina Gericke** and **Lisa Rämisch**.

Last but not least, the two people that "working from the shadows" make the division work: **Patrik Wirgin** and **Estephania Lira**. Thanks for the help during these years, and best of luck with the new PhDs at the division. Please have good care of them as you did for me.

Model catalysts studied by x-rays, visible and infrared light

Introduction

"The more I learn, the more I realize how much I don't know."
-Albert Einstein-

Background

Since the time in which alchemy was beginning its transition to the science of chemistry during the Age of Enlightenment, there were known some unique materials which had the propriety of, thanks to their presence, allowing the transformation of a substance into something else [1]. While these first unwittingly observations of catalysis can be dated back to the second half of the 18th century, it will have to wait until 1835 with J.J. Berzelius [2], to have a first and rudimentary definition of the term itself.

With its roots in the Age of Enlightenment and developing parallel to the industrial revolution, the importance of catalysis grew slowly until its almost literal explosion, in the revolutionary synthesis of ammonia at the beginning of the 20th-century [3]. This process fed both Europe and the world, thanks to the artificial fertilizers derived from it. At the same time, though, from the 1910s to 1950s, also fuelling the first and second global conflicts thanks to the manufacturing of explosives, produced from the same nitrates used for agriculture. Mainly thanks to these two contributions and much more since then, catalysis has cemented its position in an increasingly industrialized world. For these reasons, since after WWII, a great deal of money and resources has been put into catalysis resulting in countless achievements, numerous Nobel prises [4–9], and a major impact worldwide [10].

Nonetheless, a unified theory and complete understanding of the catalytic processes is still lacking due to its complexity. During the years, the catalysis community focused more and more on what today is recognized as the most relevant part for a catalyst: the *active sites* that are on the *catalysts surface* [11]. Using *Surface Science* characterization tools, in between chemistry and physics, the aim is to catalog and study various catalytic phenomena at the interface between catalysts and reactants. With atomic precision, the goal is to understand the mechanisms behind it to ultimately engineer the catalyst for the future.

Due to the complexity of catalytic systems combined with technical limitations, a common approach in catalytic surface science studies is the use of so-called *model system.* These normally consist of simplified catalysts, performing simple chemical reactions at low pressures. The advantage of this approach is the relative simplicity of of both data acquisition and analysis, often allowing to obtain atomistic overview on the process itself. Unfortunately, by definition, the condition at which the process is studied can considerably vary from the industrial process at which its originally connected to. This discrepancy between "real world" applications and scientific investigations takes the name of *material and pressure gaps* [12, 13].

Nowadays, pushing the state-of-the-art consists of mainly two approaches: first is pushing technical limitations with new and innovative techniques, second is the investigation of new catalytic materials aiming to reveal another piece of the puzzle of catalysis as a whole.

This work

This work will present a combination of both technical developments and material investigation and it will be divided into four main sections, introducing the relevant topics treated in the included publications.

Chapter 1 is focused on introducing crystals and important crystallographic concepts and jargon.

Chapter 2 will introduce important chemical notions such as *activation energy* and *chemical pathway* as well as treating general concepts about gas-surface interaction. It will also be given some information on oxidation processes, and a few paragraphs about relevant reactions such as CO and CH_4 oxidation will conclude the chapter.

Chapter 3 will be the most important and detailed of the ones presented. It will explore both theory and experimental setups for the various methods used in this work: from general proprieties of light-matter interaction and their implications to synchrotron light and specific techniques. Both diffraction and spectroscopy methods will be presented, with a short paragraph about supporting theoretical calculations.

After a short introduction to each publication in Chapter 4, the final Chater 5 will present the conclusions, along with some suggestion for the future work.

Publications

This Ph.D. work is focused on both technical and new material challenges in their own rights.

On the one hand, using well-known catalysts and reactions, such as CO oxidation using Pd model catalysts, we implemented complex experimental setups to combine x-ray, visible, and IR light. In **paper I** we performed a quantitative study on single crystal Pd(100) oxidation with a combination of HESXRD, XRR, and 2D-SOR technique, showing a remarkable sensitivity of the optical method, with resolution up to 2-3 Å in thickness measurements. In **paper III** we present the setup used in **paper I**. Here, combining HESXRD, 2D-SOR and PLIF we could also confirm previous findings [14–16] reinforcing the case for the use of multi-technique investigations while dealing with *operando* studies.

In **papers II, IV** and **V**, using CO oxidation on Pd(100) model catalyst, we tried to push the envelop of the "high pressure" in HP-XPS, presenting results obtained from few hundreds to a thousand millibar of total pressure. In specific, in **paper V** we discuss the experimental setup at beamline P22. Here it is highlighted the importance of inclusion of evanescent wave integration for data acquired at extremely low angles while at the same time confirming previous findings on metal island formation on PdO during reduction. In **paper IV** we present high resolutions HPXPS results, at near stoichiometric conditions, for CO oxidation on Pd(100) at 1 bar of total pressure. In **paper II** we present results for HPXPS of the same system presented in **paper IV** in lean conditions, integrating important experimental variables from both **paper V** and **paper IV**, and presenting interesting results for CO oxidation at highly non-stoichiometric conditions.

In **paper VI** we present some developments on a new approach to x-ray diffraction, and nominally consisting in normal incidence Transmission Surface Diffraction (TSD) by use of very thin substrates. We followed *in-situ* and *operando* the oxidation on Rh nanoparticles (NPs) and thin film and the results show that it is indeed possible to record thin oxide formation in transmission geometry. Specifically, this technical development aims to solve thermal expansion misalignment issues, typical of grazing incidence geometry experiments and at the same time enhancing the spatial resolution through the use of tightly collimated x-ray beams.

In **papers VII, IX** and **VIII** we instead investigated a relatively novel system such as Ir/IrO_2 and it's proprieties during oxidation as well as CO/CH_4 titration. To do so we employed both HESXRD and XPS to study both morphology and chemical states of the surface. Specifically in **paper VIII** we present high resolution core-level spectroscopy (HRCLS) results on IrO_2/Ir(100) correlated with Density Functional Theory (DFT) studies. In **paper IX** we present the APXPS results from CH_4 titration of IrO_2, in combination with DFT calculation. We observe efficient oxidation of CH_4 with consequent reduction of the oxide. A suggestion for an oxidation reaction path is provided from the data collected, supported with DFT calculations.

Finally, in **paper VII**, we present our HESXRD findings on morphology and epitaxy of IrO_2/Ir(100). Showing a more complex behaviour of the sample than previously expected, and correlating it with O_2 pressure. Furthermore, we conclude that this system is unfortunately worse suited for model catalysts studies if compared to similar layered systems such as IrO_2/RuO_2 [17].

1. Crystals and crystal surfaces

> *"That which is Below corresponds to that which is Above,*
> *and that which is Above, corresponds to that which is Below,*
> *to accomplish the miracles of the One Thing"*
> *-Emerald Tablet, Hermes Trismegistus-*

As we will later see, in heterogeneous catalysis the nature of the catalytic process is directly correlated to the atomic structure at the surface [15, 18] so that an introduction to crystals, crystal surfaces and some symmetry concepts is needed.

For this reason the current chapter will shortly present the proprieties of crystalline materials, what defines a crystal, and will give important crystallographic definitions relevant for later discussion.

1.1 Crystalline materials

A **perfect crystal** is, by definition, a material in which the atomic structure is constituted of atoms arranged in a perfect 3D lattice. This lattice itself is a semi-infinite repetition of a primitive unit called *unit cell*, which characteristic consists in filling completely the 3D space simply by rigid translation along its *crystalline directions*, also called *basis vectors.* [19].

Crystalline materials are generally defined as those substances that are constituted of crystal phase. They are named differently depending on the number and/or dimension of the perfect *crystal grains*, or *crystallites*, that constitute them. *Single crystals* are only those materials that are constituted by a single, uninterrupted crystal grain. While, in case only a limited ensemble of crystallites are present, the material will be named *poly-crystal.* Finally, in the case of a high number of statistically random distributed grains, the sample is defined as *powder-like.* [20]

In this work we will focus mainly on metallic single crystal as model catalysts of Pd and Ir, with only **paper VI** treating Rh film and NPs grown on MgO substrates. Crystal morphology and evolution will become apparent during

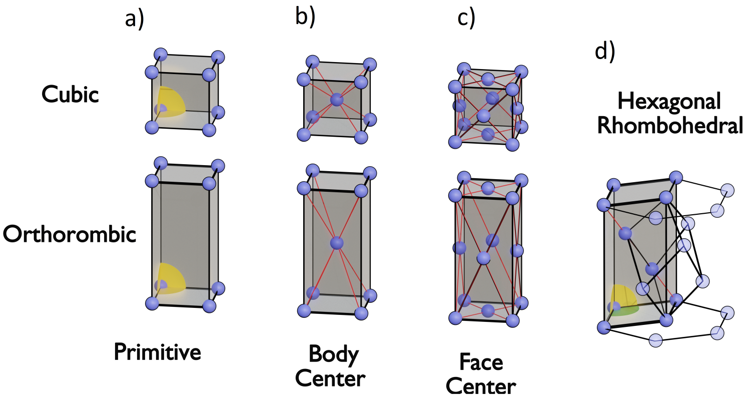

Figure 1.1: *Cubic and orthorombic crystal families with in a) Primitive b) Body-centred and c) Face-centred Bravais lattices schematically shown. Cubic lattice have all vectors* $a = b = c$ *and angles* $\alpha = \beta = \gamma = 90°$*, orthorhombic* $a = b \neq c$ *and angles* $\alpha = \beta = \gamma = 90°$*. d) rhombohedral-hexagonal Bravais lattices with basis vectors* $a = b \neq c$ *and angles of* $\alpha = \beta = 90°, \gamma = 120°$*. Angles of 90° highlighted in yellow, and 120° in green.*

oxidation and reduction cycles with the use of *in-situ* HESXRD, where the polycrystalline as well as some powder-like oxides formation will be shown in **paper I , VII, III**.

1.1.1 Crystals and symmetry

Given the crystal characteristic of 3D semi-infinite repetition, it follows, for geometric restrictions, that there are only a limited number of "shapes" for crystal unit cells that can be periodically translated to constitute the crystal itself. These distinct groups, 14 in a total, divided in 7 families, take the names of *Bravais Lattices.* Analogously, given the 14 Bravais Lattices and so-called *symmetry operations* such as rotation, translation, etc., there are only a limited number of ways a certain set of points can be re-arranged inside the cell without being identical to some other given disposition. All the possible lattices can then be subdivided into 230 different *Space Groups* each of which with unique symmetry. This will become especially relevant during acquisition and reconstruction of x-ray diffraction data, since given this inherent symmetry in the cell, we will be able to reduce the amount of data needed in order to be representative for the whole system. [19, 20]

Given the materials used in this work, such as the *transition metal* Pd, Ir, Rh and their oxides, the groups of interest will be group 225, 131 for Pd and PdO, group 225, 136 for Ir and IrO_2, and 225, 167 for Rh and Rh_2O_3.

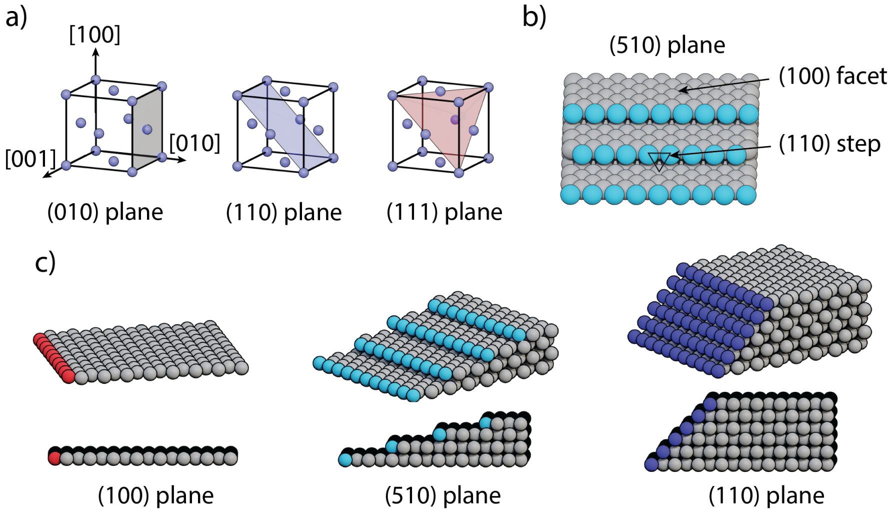

Figure 1.2: *a) Low index crystal planes visualized on a single lattice unit with b) perspective and side view of (510) vicinal surface with highlighted step and terraces. c) Side and orthogonal view of generic (100), (510) and (110) FCC facets to emphasise their relative inclination.*

Group 225 is the *Face Center Cubic* (FCC), in fig. 1.1c), along with group 229 *Body Center Cubic* (BCC), in fig. 1.1 b), one of the two most common crystal structure for transition metals and as previously said, all metallic Pd,Ir and Rh are FCC metals with cubic cell. PdO, along with IrO_2, have an orthorhombic unit cell, with slightly different subset of symmetry operations. PdO belongs to group 131 while IrO_2 to group 136. Rh_2O_3 is a corundum crystal, with an Hexagonal Rhombohedral crystal structure and a trigonal unit cell belonging to group 167, as shown in fig. 1.1d).

1.1.2 Crystal surfaces

Now, considering a crystal surface or *crystal facet*, this can also be uniquely identified indexing its orientation with respect to crystal lattice and *basis lattice vectors* and this is made with the use of so-called *Miller indexes*. Given an arbitrary plane cutting the fundamental unit cell, the Miller indexes for the plane are calculated multiplying the fractional distance between origin and point of intersection (for every basis vector) by the minimum common multiple of all the vector distances so that integer indexes values are always obtained [1].

---

[1] As a practical example, if a plane cuts at h,k,l=($^1/_3$,$^1/_4$,1) it will then have Miller indexes of (4,3,12)

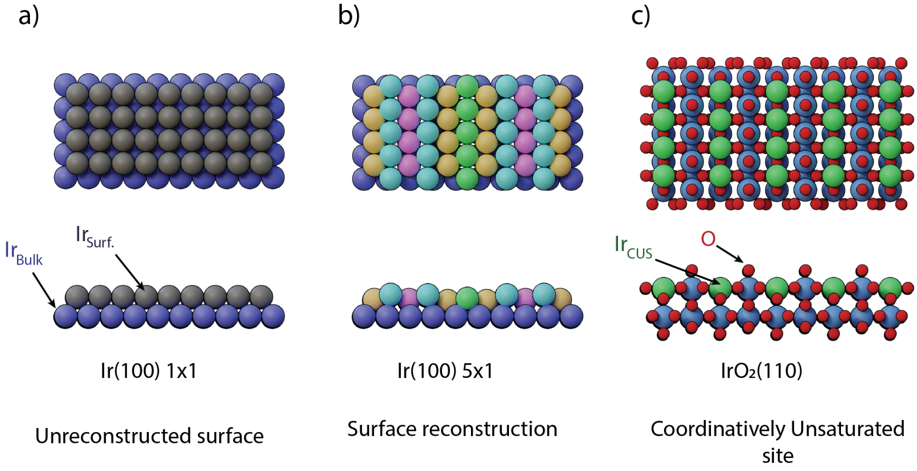

Figure 1.3: *a) Unreconstructed Ir(100)-(1x1) surface b) Reconstructed Ir(100)-(5x1) surface c)* $IrO_2(110)$ *with highlighted* Ir_{CUS} *sites (in green) and the bridging oxygen*

Moreover and by convention, depending on the kind of brackets in which these indexes are enclosed, they can indicate either a single plane family, in case of "()", all symmetry-equivalent family of planes by "{}" or the direction perpendicular to the plane with "[] ". The surfaces with lower miller index such as 100/110/111 take the name of *low index surfaces* while *high index surfaces*, or *vicinal surfaces*, will have progressively higher numbers the shallower the dihedral angle [2] of the crystal plane with respect to the main crystallographic directions. Few examples of low and high crystal surfaces for FCC crystal can be seen in fig. 1.2. Fig. 1.2a) shows low index plane, while 1.2c) present (100)/(510)/(110) planes and their respective orientation. Fig. 1.2b) shows an example of the characteristic terrace-step interval found in the vicinal surface.

Until now the surface has been considered only from a crystallographic point of view, as a perfect extension of the crystal lattice present in the *bulk*. Contrary to these bulk atoms though, which electronic proprieties can be considered perfectly identical, the surface belongs to a truncated part of the crystal lattice by definition and as such it exhibits slightly inferior electronic density. These surface atoms, due to the lack of this *electronic valence*, are then defined as *Coordinatively UnSaturated* (CUS). In particular, most relevant for crystal structures, is that this difference in electronic valence often require a different crystal cell in order to be energy stable, consequently *reconstructing* the surface to compensate.

This phenomenon takes the name of *Surface Reconstruction* and it has been

---

[2] For dihedral angle is intended the solid angle between two planes of interest

observed for a number of conditions and materials [21–23] with important consequences on many *chemical reactions at surfaces* [11]. Example of un-reconstructed and reconstructed [24, 25] surface for Ir(100) is shown in fig. 1.3a) and b), while in fig. 1.3c) is presented a relevant oxide surface structure with highlight on the Ir_{CUS} sites [26, 27]. Finally, since these reconstructions formally alter the surface symmetry, a unique *superstructure* with its *surface cell* must be identified. This will then be defined according to the so-called *Wood's notation*[28].

Relevant for this work are mainly low index facets of metal oxides and their *epitaxial relationships* to the surface, that is, the relative crystal orientation between the different phases present in the system.

2. Gas-surface interaction

"God made the bulk; surfaces were invented by the devil."
-Wolfgang Pauli-

While the previous chapter focused on crystallographic concepts, this section will focus on interaction between surfaces and gas-phase introducing some fundamental concepts on thermodynamics and kinetics.

As a simple introduction to catalysis, and to illustrate its use in chemical reactions, we can write one of the most critical reactions in the field [29] , as well as a central reaction for this work: CO oxidation.

The CO oxidation reaction can be written as:

$$\begin{array}{ccccc} \text{Reactants} & & \text{(Transition states)} & & \text{Product} \\ CO + \frac{1}{2}O_2 & \rightleftharpoons & (CO^* + O^*) & \rightleftharpoons & CO_2 \end{array} \tag{2.1}$$

Formula 2.1 indicates the chemical reaction between the reactants, through *transition states*, to the products. The "$\rightleftharpoons$" symbol indicate the *thermodynamic* equilibrium between the reactants and products according to *Le Chatelier's principle* [30]. Depending on the relative energy/stability of the chemicals on either side of the formula, the reaction will reach an equilibrium state based on the lowest overall energy configuration. These energy considerations, the *thermodynamics*, will tell us the overall equilibrium state but nothing about the rate at which the reaction takes place, or the *kinetics*, of the process. [2]

In this regard, CO oxidation is, yet again, an excellent candidate to highlight the importance of kinetics considerations. Is then shown in fig. 2.1 how the CO oxidation thermodynamics is heavily biased towards CO_2, but due to the high stability of the C-O and O-O bonds they require considerable energy in order to be broken so that this *activation energy* would practically block the reaction. As schematically shown in fig. 2.1, then the catalyst role is then to provide alternative intermediate states, with lower activation energy barriers between

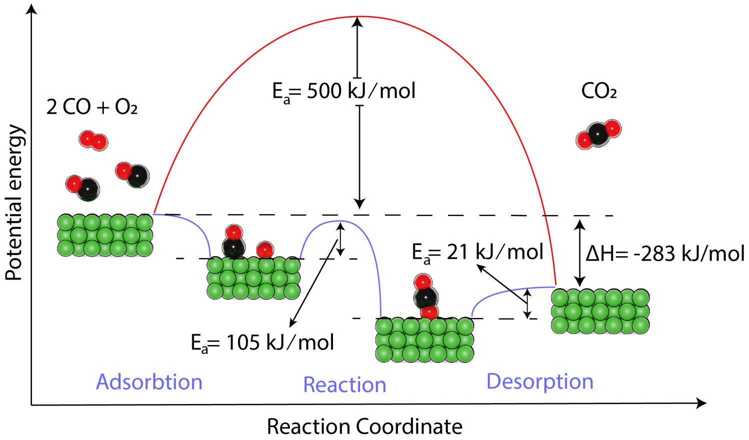

Figure 2.1: *Potential energy diagram for CO oxidation over a catalyst surface. The reaction path is shown for the cases without (red) and with a catalyst (blue). The indicated energy values correspond to a reaction via the Langmuir-Hinshelwood mechanism on Pt(111), assuming low surface coverages [31].*

them. This newly created *reaction path* between reactants and products will consequently yield higher energy efficiency, allowing it to occur several orders of magnitude faster than otherwise possible.

2.1 Heterogeneous Model Catalysts

Generally, catalysts can be classified in two broad sub-categories: *homogeneous* and *heterogeneous*. The terms are referred to the physical states of the catalysts respect to the reactants/products in which they are operating [32]. A homogeneous catalyst is in the same physical state as the reactants/products. This class of catalyst is extensively used in organic chemistry and industry but well outside the scope of this work. Heterogeneous catalysts, like the ones used in this work, are catalysts present in different phases compared to the reaction chemicals.

This work will specifically focus on gas-solid heterogeneous catalysis. Particularly, this work will focus on *model catalyst* [33] to distinguish it from the industrial standard of multi-material, multi crystalline and not homogeneous material system [32].

Model catalysts can be broadly defined as simplified systems that, approximating industrial catalytic conditions, try to bridge the *material and pressure gap* between real-world application and instrumental capabilities for scientific analysis, schematically represented in fig. 2.2. In this work the model will consist

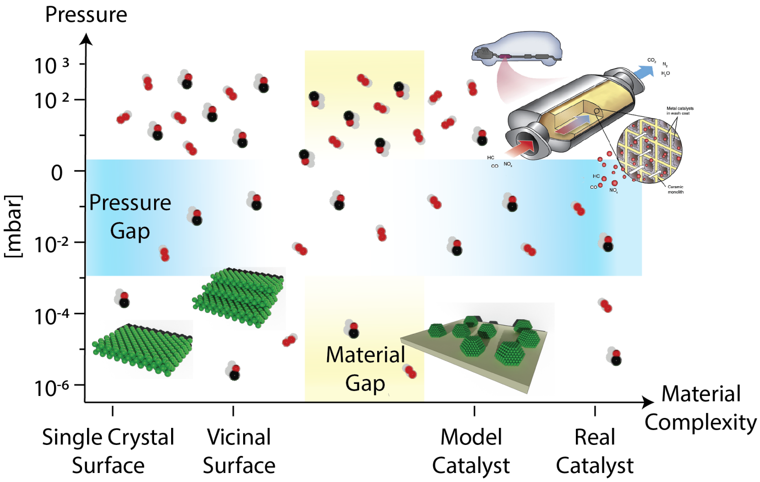

Figure 2.2: *Overview of the phase space of materials and pressures for catalysis research. While real catalysts operate at up to tens/hundreds of bars, with a high degree of material complexity (upper right corner of the diagram), research typically happens for simple and idealized systems (lower left corner). The figure illustrate the origin of the pressure and material gaps, which is an important goal of fundamental catalysis research to bridge*

mostly of metal single-crystals, Pd(100) and Ir(100) or hepitaxial Rh(100) thin films, that consequently will expose only a single crystal facet to the reaction. In minor part also Rh NPs will be studied as benchmark for instrumental capabilities. For what concern the catalytic reactions, they will be performed at slightly lower pressures than industrial conditions, up to a few hundred millibars in most cases.

The model catalyst approach will then significantly reduce the variable space available and facilitate experimental interpretation and theoretical modelling of the catalyst/reaction system.

2.1.1 Gas-Surface Interaction

As previously introduced, the role of heterogeneous catalysts is to provide a different reaction pathway, specifically interacting and stabilizing molecular/atomic transition states onto their surfaces. Depending on the electronic affinity between molecular/atomical species and the surface, and their interaction energy, multiple intermediate states and electronic interactions are possible. These interaction can be then classified in three main categories depending on the type of chemical bond and the associated interaction energy. In case of Wan-der-Waals interaction or hydrogen bonds, with typical interaction energy weaker than roughly 2 eV, the interaction is called *Physisorption*. In case of covalent or ionic bonds that do not brake the original species apart, and with energy between 2 eV and 10 eV, is called

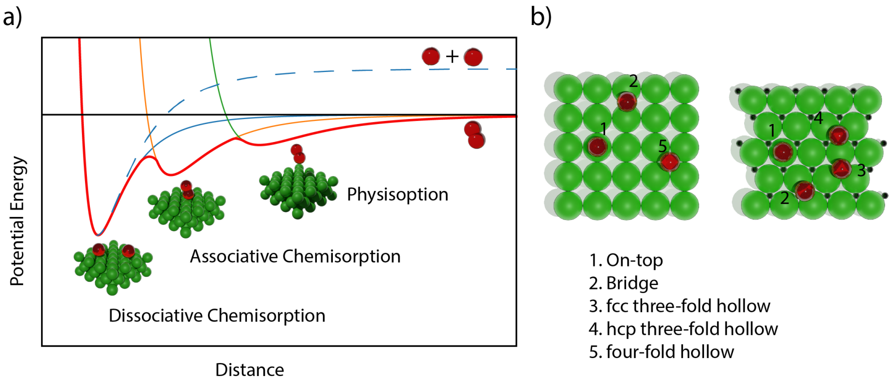

Figure 2.3: *a) Example of a Lenard-Jones [31] energy potential diagram for different adsorption mechanisms of a gas molecule on surfaces. b) Different adsorption sites on (100) and (111) FCC metal surfaces.*

Associative chemisorption. Finally, when the surface interaction brakes the original species and with typical energy above ~10 eV *Dissociative chemisorption*[31] . A schematics of the energy potential for the three interactions and for a generic diatomic molecule is displayed in fig 2.3a).

One of the factors that can influence this interaction, apart from material and surface morphology, is the position on the surface in which this takes place. This is because the *chemical coordination* of every single *surface adsorption site* will greatly vary depending on the surrounding, as also mentioned for CUS sites in sec. 1.1.2. For unreconstructed surfaces, based on the number of surface atoms involved in the adsorption process and the following geometry, the *interaction site* can be classified as: *atop*, *bridge*, *3-fold* or *4-fold* when interacting with respectively one to up to four atoms on the surface, as seen fig. 2.3b) [28].

For reconstructed surfaces, more complicated geometries can arise, and they are more complex to classify. One of such geometries relevant for this work is the aforementioned CUS site, that can be seen in fig. 1.3c) for IrO_2. As the name implies, this *catalytic-active site* presents unsaturated metallic atoms at the surfaces, which presenting a local difference in electronic valence, shows enhanced catalytic proprieties compared to otherwise electronically saturated surfaces. CUS sites can be found particularly in step-sites of metals, oxide-metal interfaces as well as in oxide structures such as RuO_2 [34, 35] ,PdO [15, 36] or IrO_2 [37] where a ridge formation of missing oxygens can be present at specific facets, as for instance for (110) on rutile structures. [38].

As far as the reactions mechanisms on the surface are concerned, and independently on the adsorption site which will be specific for any reactions/catalyst/pressure combination, the chemical reaction can occur following three broad reaction mechanisms that encompass all possible alternatives: *Langmuir-Hinshelwood*, *Elay-*

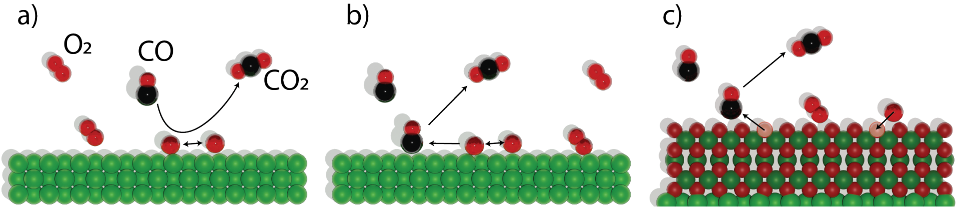

Figure 2.4: *Diagram of different reaction mechanisms for CO oxidation on a heterogeneous catalysts. From left to right a) Elay-Rideal, b) Langmuir-Hinshelwood and c) Mars-van-Klevelen mechanism*

Rideal or *Mars-van-Klevelen* [3]. The Elay-Rideal mechanism, 2.4 a), consists in the reaction between one adsorbed reactant and one from the gas phase. The Langmuir-Hinshelwood mechanism, in fig. 2.4 b), sees all the reactants to be adsorbed on the surface first, either molecularly or in a dissociative fashion, and only after reacting between the adsorbed species. Lastly, the Mars-van-Klevelen mechanism in 2.4 c), requires the presence of an oxide surface onto which the reactants can adsorb and subsequently react with the oxygen atoms from the oxide layer.

2.1.2 CO Oxidation

CO oxidation is one of the most critical reactions in catalysis, for both scientific and industrial applications[39], and it has been subject to extensive studies over several decades. Its relative simplicity, involving two of the most basic and important molecules in nature, combined with the ubiquity and usefulness of the process, makes it a cornerstone in chemistry. For these reasons, CO oxidation is today considered a major benchmark for catalytic surface science studies, as far as being defined as the *prototypical* catalytic reaction [29].

Is important to remark though, that depending on the catalytic surface and experimental conditions, the CO oxidation is reported to proceed by different mechanisms. On metallic Pd(100) [40] or Pd(111) [41] for instance is concluded to oxidize with Langmuir-Hinshelwood mechanism. On oxidized samples as the rutile oxides RuO_2 [38] and PdO [42] is reported to react by Mars-van-Klevelen mechanism, even though it has also been suggested reacting with Elay-Rideal mechanism on PdO(101) [43].

In this work CO oxidation reaction has been used, on Pd(100) model catalyst, in **paper II, III, IV** and **V** with a combination of diffraction and spectroscopic techniques.

2.1.3 CH_4 Oxidation

Methane oxidation, and specifically direct partial methane oxidation, sits at the opposite spectrum compared to CO oxidation and is nowadays considered a sort of "holy grail" of catalysis [44]. Methane, formula CH_4, is highly abundant and cheap, coming from several sources ranging from bio-methane [45] to a by-product of oil drilling [46]. Conversely, its partial oxidized derivatives are a fundamental building block for most of the chemical industry, although being relatively expensive to produce. The straightforward solution would be to react the excess CH_4 into added value product, but unfortunately, due to the extreme chemical stability of the C-H bond in methane [47] nowadays, there are no known direct pathways for $CH_4 \rightarrow CH_xO_y$.

For this reason, and due to recent surge of interest, part of this work has been focused on the study of CH_4 oxidation and characterization of its known most efficient catalyst to date: IrO_2 [26].

In particular **paper IX** presents a preliminary study of CH_4 titration of IrO_2, studied by HPXPS, but further studies are still ongoing.

2.2 Oxidation of catalysts

As also discussed above, understanding the proprieties of metal and metal oxide catalysts, including the oxidation/reduction process at the surface and resulting morphology changes are of primary importance to characterize the overall reaction mechanism. For this reason, part of this work has been dedicated particularly to the analysis of catalysts oxidation process and its consequences at the surface.

Chemisorption and surface oxide formation

The first step for a metallic sample, before the oxidation, is the chemisorption of the oxygen onto the surface (formal definition in section 2.1.1). Given the unstable nature of metallic surfaces as they are, this step may result in a surface relaxation, "lifting" metal atoms out of the bulk into a reconstructed form. Depending on the type and amount of gas present, more or less dense reconstructions/superstructures will be formed. The resulting gas coverage is usually reported in *Mono Layers* (ML), which can be estimated by the crystallographic considerations once the surface structure has been determined, and in which 1 ML will be defined here as the number of gas molecules equivalent to the metallic surface atoms.

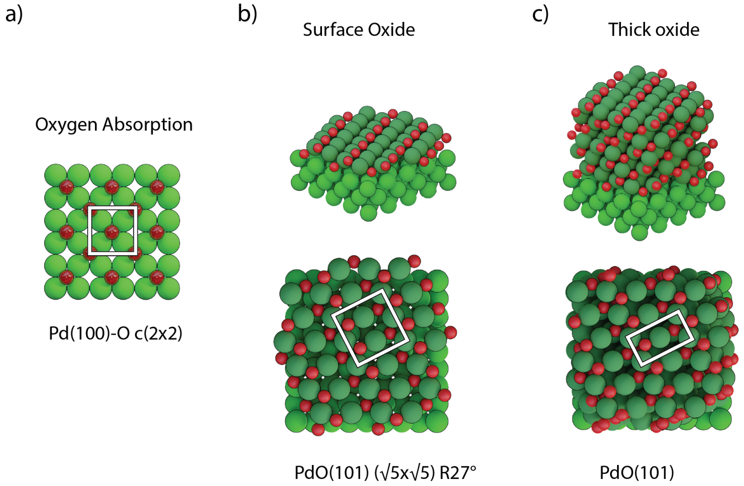

Figure 2.5: *a) Surface reconstructions for oxygen on c(2x2)-Pd(100) at 0.5 ML. b-c) top and side view for* $(\sqrt{5} \times \sqrt{5})R27°$*-PdO(101) and bulk-PdO(101). The unit cells are highlighted as white squares.*

Some example of such reconstructions are the PdO(100)-O c(2x2) at 0,5 ML [48], shown in fig. 2.5a), similar to what was observed on Ir(100)-O c(2x2) in **paper VII**.

Second stage in oxidation process is the formation of so called *surface oxide* of *thin oxide* [49]. Given the quasi-2D nature of this oxide, and similarly to what happens for metallic surface reconstruction, to stabilize the oxide its unit cell "relaxes" and deforms to better fit the underlying metal. The resulting combination of surface oxide and underlying bulk component then generates a so-called *super lattice cell.* When multiple oxide layers are deposited, at later stage of oxidation, the oxide crystal cell will stabilize and coincide with the *commensurate* oxide bulk cell.

Example of this oxidation process is clear on Pd, were the $(\sqrt{5}\text{x}\sqrt{5})$ R27° - PdO(101) [50], shown in fig. 2.5b), is formed at low O_2 pressures and prior to bulk oxidation. On a later stage of the oxidation process, the $(\sqrt{5}\text{x}\sqrt{5})$ R27° form disappears, and only the bulk PdO(101), fig. 2.5c), remain visible [14].

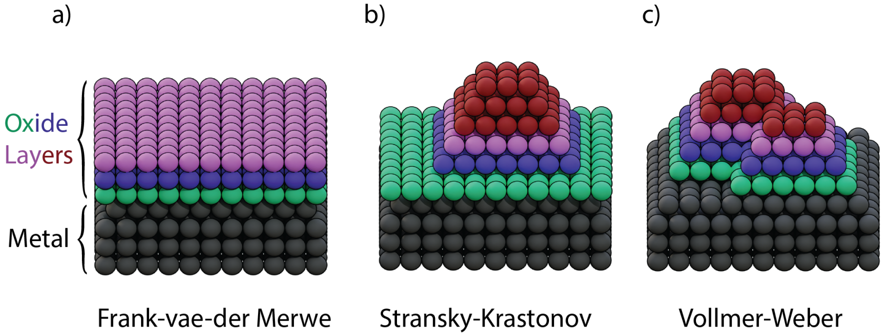

Figure 2.6: *Oxidation mechanisms for bulk oxides. a) Frank-van-der-Merwe, with a layer by layer growth. In b) Stranski-Krastonov, with initial total wetting of the surface followed by island growth on top. c) Vollmer-Weber, with island growth and minimal wetting of the metal surface.*

Bulk oxide formation

After the transitions from surface to bulk oxide and beyond crystallographic considerations, it is important to notice that the force of the oxidation will often physically modify the morphology of the surface on μm scale [28]. This process of oxide thickening can be generally classified into three prominent families [3] depending on the resulting surface, and which layering can be seen from fig 2.6.

The "simplest" of these arrangements is a layer-by-layer stacking in which the oxide will try to *wet* (cover) the surface evenly: this atomistic model, shown in fig. 2.6a), takes the name of *Frank-van der Merwe* growth. The second kind of atomic behaviour, at the opposite side of the spectrum, is when the oxide wets as little surface as possible, forming *oxide islands* on the surface, as shown in fig. 2.6c). This growth model takes the name of *Vollmer-Weber*. Lastly, taking the name of *Stranski-Krastonov*, in fig. 2.6b), is a mixture of the prior two modes: with the oxide forming some layers at first and subsequently developing islands on top of that. This last oxidation mechanism is what commonly occurs in in PdO/Pd(100), as observed also in **paper I and V**.

Important note is that the oxidation process can generate several relatively stable oxide phases and/or facets at the same time, which equilibrium will highly depend on many thermodynamic factors such as pressure, temperature, *interfacial energy* between different *epitaxial orientation*, etc. In **paper VII** we encounter such behaviour and we present a detailed analysis of IrO_2/Ir(100) facets and hepitaxis, clearly showing the delicate and metastable equilibrium just described.

Oxide reduction

The reduction process of the oxide to the original metallic form can happen for both *thermal decomposition* of the oxide, as well as through the use of reducing agents such as H_2, CO, CH_4 etc.

Similar to what happened for the oxidation, the reduction process begins from the oxide surface forming metal islands [36] on top of it and resulting in a multi-layer Metal-Oxide-Metal structure.

This relatively recent insight could be of particular interest, since peculiar synergy effects in enhancing catalytic activity are known in mixed metal catalysts [51, 52].

Moreover, in **paper VII** on IrO_2/Ir(100) system the morphology resulting from the newly reduced sample shows the presence of metallic island on top of the original metallic substrate, with preference for a specific facet island orientation.

3. Methods

> *"I think that modern physics*
> *has definitely decided in favor of Plato.*
> *In fact, the smallest units of matter*
> *are not physical objects in the ordinary sense;*
> *they are forms, ideas which can be expressed*
> *unambiguously only in mathematical language."*
> *-Werner Heisenberg -*

This work's main investigation toolbox has been based on several light-matter interaction techniques, ranging from x-ray diffraction (XRD) to x-ray and laser spectroscopies. Moreover, whenever possible, a multi-technique approach has been used to acquire information with orthogonal investigation methods for the correlation of surface and gas-phase signals and methodological validation. Furthermore, on few occasions the experimental results have been coupled and confronted with theoretical calculations to extrapolate overall reaction mechanisms.

After a general introduction to relevant light-matter interaction phenomena, the first part of the chapter will be dedicated to synchrotron and x-rays based techniques. The following sections will be dedicated to non-x-ray methods such as Surface Optical Reflectance (SOR) and Planer Induced Fluorescence (PLIF), with a short closing paragraph about computational methods such as Density Functional Theory (DFT).

3.1 Light-matter Interaction

The unified nature of different *electromagnetic waves* (EM) such as radio waves, visible light and x-rays, schematically visualized in fig. 3.1, can be expressed by two principles, both dated to the beginning of the 20^{th} century, such as Planck relation and the De-Broglie principle [19].

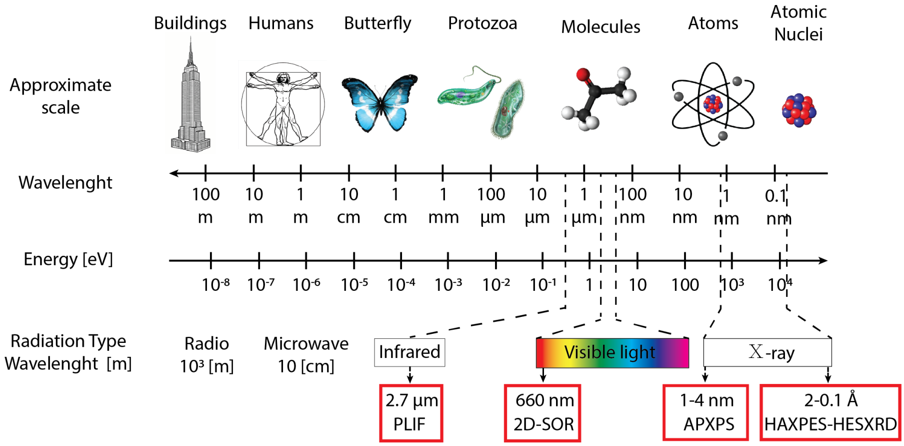

Figure 3.1: *Schematic visualization of electromagnetic spectrum from radio to γ-rays. Important quantities, such as wavelength and photon energy is provided. At the bottom is reported an approximate wavelength the methods used in this work.*

The first formulation of Plank's relation, in 1900, can be written as:

$$E = h\nu = \frac{hc}{\lambda} \tag{3.1}$$

Followed after few years by the De-Broglie principle formulated as:

$$\lambda(\text{Å}) = \frac{h}{c \cdot E} \approx \frac{12400}{E[\text{eV}]} \tag{3.2}$$

where in both h is the Plank constant, ν is the light frequency and c the speed of light.

These two formulas unify many experimental observations under the concept of a continuous EM spectrum and establish a direct correlation between energy and wavelength.

According to formulas 3.1 and 3.2, and as can be seen in fig. 3.1, the typical energy range of x-rays is between 1 keV and 100 keV, corresponding to a wavelength of 12 and 0.12 Å. With atoms whose dimensions are in the Å range, it will be shown how the use of this wavelength allows atomic diffraction phenomena while at the same time, due to the high energy associated with the radiation, this also enables investigation of atomic core-level spectroscopic phenomena. Lower in energy and employed in 2D-SOR, we use visible light in the range of a few hundred nm taking advantage of optical reflectivity of the surface. Finally, at lower end of the energy spectrum, IR light in the micron range is used molecular spectroscopy targetting CO_2 molecules by means of PLIF.

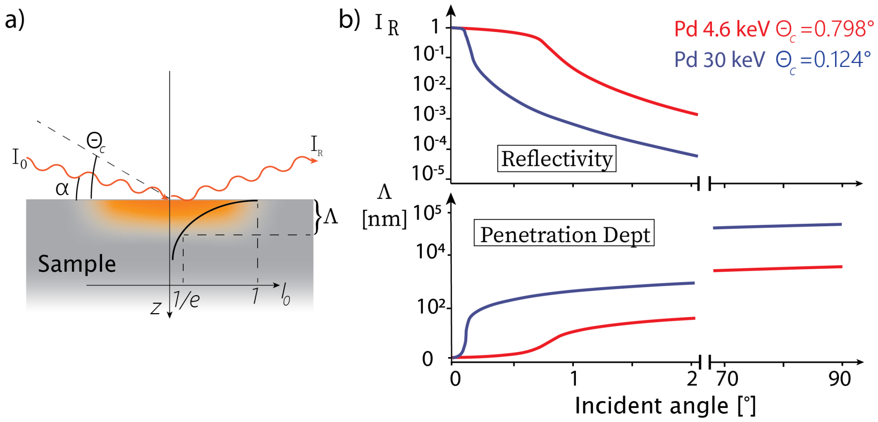

Figure 3.2: *a) Schematic representation of total external reflection. In the sample (grey) is highlighted the volume of the evanescent field (orange) and its intensity respect to depth, with definition of penetration depth Λ. b) Angle dependent reflectance and penetration depth curves for Pd at lower and higher energy.*

Refractive index

Considering the energy/wavelengths range employed, the treatment of some optical proprieties of the material investigated will be essential in the following discussion. Primary among these is the refractive index n expressed as:

$$n = 1 - \delta + i\beta$$
$$\delta = \frac{n_a r_e \lambda^2}{2\pi} \cdot f_1 \qquad \beta = \frac{n_a r_e \lambda^2}{2\pi} \cdot f_2 \tag{3.3}$$

Combining eq. 3.3 with Snell's law:

$$n \cos\theta = n' \cos\theta' \tag{3.4}$$

a *critical angle* Θ_c can be expressed as a function of δ, $\theta' = 0$ so that $\theta = \Theta_c$:

$$\Theta_c = \sqrt{2\delta} \tag{3.5}$$

The critical angle Θ_c is then based on the real part of the refractive index n, referred to as δ, and which in turn is based on electron density n_a, the classical electron radius r_e, the radiation wavelength λ and the dispersive atomic scattering factor f_1. The imaginary part of n is β and it has a similar formulation to δ with the difference being based on the abortive atomic scattering factor f_2.

With incident angle below the Θ_c the light is almost completely reflected with either *total internal/external reflection* with the side of the reflection depending on n being greater or smaller than unity [20, 53]. Given the energy dependence of n, and for x-rays in the keV range, we generally observe that the refractive index becomes less than unity with radiation undergoing total external reflection for angle $\alpha < \Theta_c$, as shown in 3.2a), .

For transition metals and light in the keV range, typical Θ_c values are smaller than 0.1°. For Pd and Ir at $\sim$ 80 keV Θ_c correspond to 0.04° and 0.06° respectively, as can also be seen for Pd case in fig. 3.2b) or from experimental X-ray Reflectivity (XRR) curve in fig. 3.10.

At angles close to the critical angle, in the transition between total external reflection and refraction regimes, a EM phenomenon know as *evanescent wave* or *evanescent field* arises [54]. This phenomenon will have repercussion on both scattering and spectroscopic techniques, and its contribution are now used in physics [55] and life sciences [56] alike in a variety of applications. In this work it will be mainly connected to the x-ray scattering, and in particular the limitation of penetration depth Λ [1]of x-rays when close to Θ_c.

Few example of reflectivity [57, 58] and penetration depth [59–61] are provided for relevant conditions in fig. 3.2b), and which implications will be become apparent in section 3.3.2 and 3.5 respectively.

3.2 Synchrotron Radiation

X-rays will be a primary investigation tool during the development of this work and although other more conventional methods of producing x-ray are commonly available, due to the high photon flux and energy tunability required for the experiments presented in this dissertation, the chose generation methods of interest is *Synchrotron radiation* [62]. For this reason this section will present a short introduction on synchrotrons, which schematic overview is shown in fig. 3.3a), and their general operation principles.

Synchrotrons are circular electron accelerators which *storage ring* contains the electrons, whose speed and relative energy will determine the energy interval of the light produced. Inside the ring, the electrons are kept in bunches at a constant speed and along the correct path using a combination of *RF cavities*, *bending magnets* and *collimators*. When passing along magnetic arrays called *insertion devices*, in the case presented a type called *ondulator*, the electron beam are forced to oscillate on their path, with the oscillation determined by the magnetic field. This wiggle motion will then produce photons by *Bremsstrahlung* effect.

The photons will propagate tangentially with respect to the ring and along which *optical path* is placed the *beamline*. This consist of *optical hutches* whose

---

[1] The penetration depth Λ is defined as the distance in the material at which the intensity of the field decays to $1/e$ of the surface value

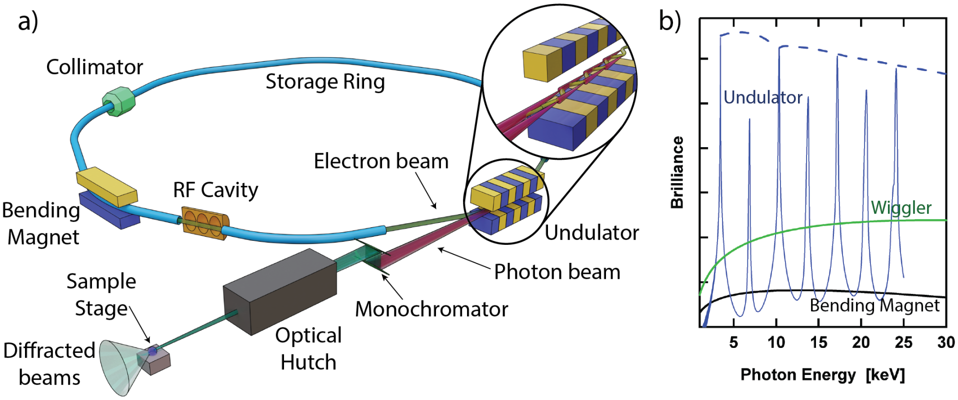

Figure 3.3: *a) Schematic representation of synchrotron facility with its most important components highlighted. In the inset: visualization of Bremsstrahlung effect inside the undulator b) Brilliance vs Photon energy for different insertion devices available at synchrotron facilities.[63]*

custom optical elements are selected based on the beamline speciality, as well as the *experimental hutch*, where the measurement takes place.

The unique scientific contribution of the synchrotron lies in the intrinsic qualities of the light produced: *brilliance* and *coherence*. Most relevant for this work is the brilliance, which is defined as photon flux per unit area, solid angle and a very narrow (0.1%) bandwidth (BW), with its formula written as:

$$\text{Brilliance} = \frac{\text{Flux}}{A_s \cdot \Delta\Phi \cdot \nabla\psi} = \frac{\frac{\text{Photons}}{s \cdot \text{BW}}}{A_s \cdot \Delta\Phi \cdot \nabla\psi} \; ; \; \left[\frac{\text{Photons}}{(s \cdot mm^2 \cdot mrad^2 \cdot 0.1\% BW)}\right] \tag{3.6}$$

where the flux is given as photon/seconds, A_s is the source area, $\Delta\phi$ is the angular divergence, and $\nabla\psi$ is the bandwidth. Where the coherence can be expressed as bandwidth generated by the light-source as $\left(\frac{\lambda}{\Delta\lambda}\right)$. [54]

A short summary of the beamlines and associated synchrotron-based techniques used are reported in table 3.1.

3.3 X-ray Diffraction

X-ray diffraction (XRD) is one of the principal investigation methods used in this work and it has been utilized for more than a century [68, 69] as one of the main tools for the investigation of both organic [70] and inorganic

Paper	Synchrotron	Beamline	Research
Paper I Paper VII Paper III Paper VI	DESY, Hamburg, Germany	P07 [64]	HESXRD TSD
Paper II Paper IV Paper V	DESY, Hamburg, Germany	P22 [65, 66]	HAXPES
Paper IX Paper VIII	NSLS II, New York, USA	23-ID-2 [67]	AP-XPS
Paper VI	ESRF, Grenoble, France	ID31	TSD

Table 3.1: *Short summary of papers associated with the synchrotron/beamline at which the experiments took place. The right hand column represent the beamline speciality, but for most of the experiments additional non-synchrotron based methods were also implemented.*

[71] crystal structure, as well as becoming a a cornerstone surface science [72]. The XRD mechanism relies on the *elastic scattering* of x-rays by the crystal periodic lattice, generating a 3D interference pattern.

This generated pattern, analogously to a simple double-slit experiment [28, 33], can yield through standardized procedures [73] a large amount of information on crystal structure and sample morphology.

In the following, some theoretical details needed for the interpretation of an XRD pattern will be presented.

3.3.1 XRD General Concepts

To analyse crystal structures we need a probe with adequate spatial resolution. This implies for crystal diffraction, and according to eq. 3.7, that a wavelength of approximately of 1 Å or smaller is needed in order to successfully probe atomic structures. From equations 3.1 and 3.2 previously presented, it then follows that the required radiation energies are the keV range, classified as x- and γ-rays.

The scattering phenomena on which XRD is based upon can be interpreted using two slightly different approaches. Although both equally valid, they present different subsets of pros and cons for the experimental framework explanation. For this reason both the semi-classical *Bragg Diffraction* approach and the individual-scatterer *Laue Diffraction* approach will be

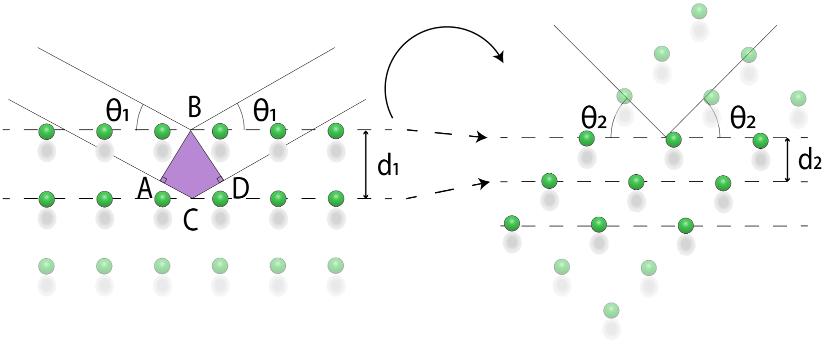

Figure 3.4: *Schematic representation of the diffraction by two parallel planes visualized according to the Bragg diffraction principles. The path difference (PD), in the left figure given by* $\overline{AC}+\overline{CD}$*, depends on the angle* θ *and the interplanar distance* d

introduced in the following [20, 54, 72].

Bragg Diffraction

The Bragg diffraction principle is based on the assumption that the incoming light will be diffracted from the crystal's atomic planes, similar to as it would be from a birefringent mirror. For visualization purposes fig. 3.4 consider a single set of planes in a 2D scenario, so we can write:

$$PD = 2d\sin(\Theta) = n\lambda \tag{3.7}$$

The Bragg diffraction law states that the difference in the optical path (PD) can be trigonometrically calculated by the interplanar distance d as the spacing given by $n\lambda$, such that diffraction spots are only produced when the two light paths show constructive interference.

Iterating this approach for every family of planes in the crystal, as seen in chapter 1, will generate a 3D distribution of *Bragg diffraction spots* with the positions uniquely identified by the sum of all inter-planar distances in the original crystal.

The main advantage of this method is the simplicity of the calculations involved that make it especially suitable for simple diffraction pattern, such as with powder samples, or "back of the napkin math" check for many chemists and physicists alike.

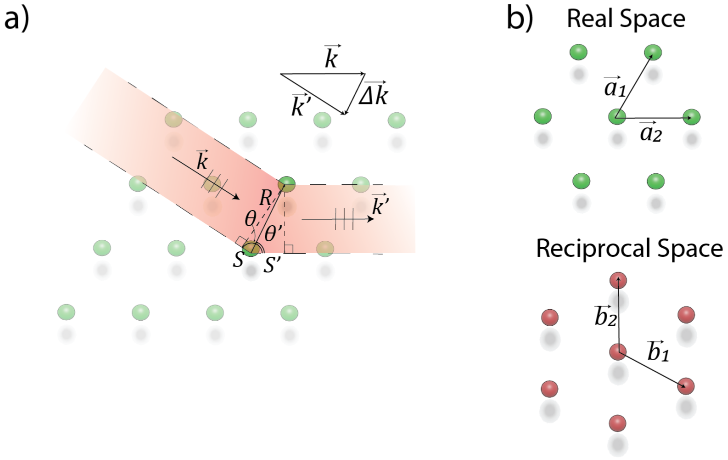

Figure 3.5: *a) Schematic representation of elastic scattering of electromagnetic radiation from two atoms, according to the Laue formulation. b) Real space at the top and corresponding reciprocal space representation at the bottom including the orientation of the base vectors* $\vec{a_1}, \vec{a_2}$ *and the corresponding reciprocal space vectors* $\vec{b_1}, \vec{b_2}$

Laue Diffraction

The Laue interpretation is based on the photon momentum transfer principle, treating the atoms as single point emitters. The vectorial interpretation is schematically presented in fig. 3.5 a).

In this model, the EM wave with *wavevector* $\vec{k}$ scatters from two atoms at a distance $\vec{R}$ from each other. Due to momentum conservation, and after the elastic scattering, the outcoming wavevector $\vec{k'}$ differs in direction with unchanged intensity and can be written as:

$$k = |\vec{k}| = |\vec{k'}| = \frac{2\pi}{\lambda} \tag{3.8}$$

The resulting momentum $\vec{q}$ is proportional to the wave vector $\vec{k}$.

$$q = |\vec{q}| = |\vec{q'}| = \frac{h}{\lambda} = \frac{h}{2\pi}k \tag{3.9}$$

with h being the Plank's constant. The condition for constructive interference based on fig. 3.5, can be derived as:

$$PD = S + S' = R\cos\theta' + R\cos\theta = \frac{\vec{R}\cdot\vec{k'}}{k} - \frac{\vec{R}\cdot\vec{k}}{k} = \frac{\vec{R}\cdot\Delta\vec{k}}{k} = n\lambda = n\frac{2\pi}{k} \tag{3.10}$$

Where the path difference (PD) has to equal an integer number of wavelengths. It follows that:

$$R \cdot \Delta\vec{k} = 2\pi n \text{ , n} \in \mathbb{Z} \tag{3.11}$$

where equation 3.11 represents the explicit condition for constructive interference.

We can then expand the case from two scatterers to an infinite crystal lattice where all the distances $\vec{R}$, written as 3D vectors as $\vec{R} = u\vec{a_1} + v\vec{a_2} + w\vec{a_3}$, that satisfy eq. 3.11 will generate constructive interference. In this case, the generic vector $\vec{R}$ is expressed as a combination of $\vec{a_1}, \vec{a_2}, \vec{a_3}$ as *orthonormal Real Space basis vectors* where u, v, w are integer numbers.

Similarly to the Bragg diffraction, and due to symmetry considerations, it can be shown [19, 20] that these scatterers will generate an infinite amount of Bragg reflections. Analogously to the real space vectors for atom positions, we can then define for the Bragg spots *reciprocal space vectors* $\vec{b_1}, \vec{b_2}, \vec{b_3}$ such as $\vec{K} = h\vec{b_1} + k\vec{b_2} + l\vec{b_3}$, which have to fulfil the bijective relationship with the real space given by:

$$e^{i\vec{K}\cdot\vec{R}} = 1 \tag{3.12}$$

The base vectors can then be constructed as:

$$\vec{b_1} = 2\pi\frac{\vec{a_2} \times \vec{a_3}}{\vec{a_1} \cdot (\vec{a_2} \times \vec{a_3})} \text{ ; } \vec{b_2} = 2\pi\frac{\vec{a_3} \times \vec{a_1}}{\vec{a_1} \cdot (\vec{a_2} \times \vec{a_3})} \text{ ; } \vec{b_1} = 2\pi\frac{\vec{a_1} \times \vec{a_2}}{\vec{a_1} \cdot (\vec{a_2} \times \vec{a_3})} \tag{3.13}$$

from which we can derive:

$$\vec{b_i} \cdot \vec{a_j} = \begin{cases} 2\pi & \text{if } i = j \\ 0 & \text{if } i \neq j \end{cases} \tag{3.14}$$

Eq. 3.14 shows that $\vec{b_i}$ is perpendicular to two vectors $\vec{a_j}$ with $(i \neq j)$ and length:

$$|\vec{b_i}| = \frac{2\pi}{|\vec{a_i}| \cos\phi} \tag{3.15}$$

with ϕ being the angle between vectors $\vec{a_i}$ and $\vec{b_i}$, with b_i measured in [Å^{-1}].

The relationship between the lattice geometry in the real space and the one in reciprocal space can schematically be seen in fig. 3.5 b).

With a relatively simple computational procedure, this vectorial interpretation will allow us to obtain detailed crystal geometry information from a recorded diffraction pattern.

The Ewald's sphere

As concluded in both diffraction approximations, the resulting scattering from a crystal will be a 3D distribution of Bragg reflections which coordinate, from Laue interpretation, will be expressed in reciprocal lattice unit [Å^{-1}]. As visible from eq. 3.11, with $\vec{k'_n} = |\vec{k}|$, the resulting construction for all possible scattering vector orientations is a sphere of radius $|\vec{k}|$.

This construction is called *Ewald's sphere* and presents two main visualization benefits. On the one hand, it will provide the accessible reciprocal space volume for a given radiation energy. On the other, it will aid in visualizing the diffraction condition.

Demonstrating the first point is rather intuitive because, given the cited diffraction condition and momentum conservation $\vec{k'_n} = |\vec{k}|$, everything beyond a $|\vec{k}|$ radius is not accessible by definition. It is also relevant considering how the sphere radius is directly connected to x-ray energy through 3.8, as can be schematically seen in fig. 3.6b), and as seen in section 3.3.2 concerning HESXRD.

To illustrate the second point about the diffraction spot visibility, it is a little less straightforward and is illustrated in fig. 3.6a) in which the Ewald's sphere surface and the desired reciprocal space lattice point overlap. Since the reciprocal space origin $(0, 0)$ must always be visible, it always lies on the sphere, thus it follows a real space rotation of the crystal results of rotation of reciprocal space around $(0, 0)$. Since the momentum conservation law require $\vec{k'_n} = |\vec{k}|$ it follows that any $|\Delta k|$ associated with a reflection must lie on the sphere itself.

A final consideration is the relative thickness of the sphere. Although considered infinitely thin until now, due to a perfect coherence in $\vec{k}$, real sources always present a small error $\delta\vec{k}$ given by the inevitable characteristic bandwidth $\nabla\psi$, as from eq. 3.6. This, in turn, contributes to generate a Ewald's sphere of non-zero δ shell thickness. Since the XRD signal intensity is correlated to the intersected volume between Bragg peak and Ewald's sphere, the chosen energy bandwidth is then an important variable to consider.

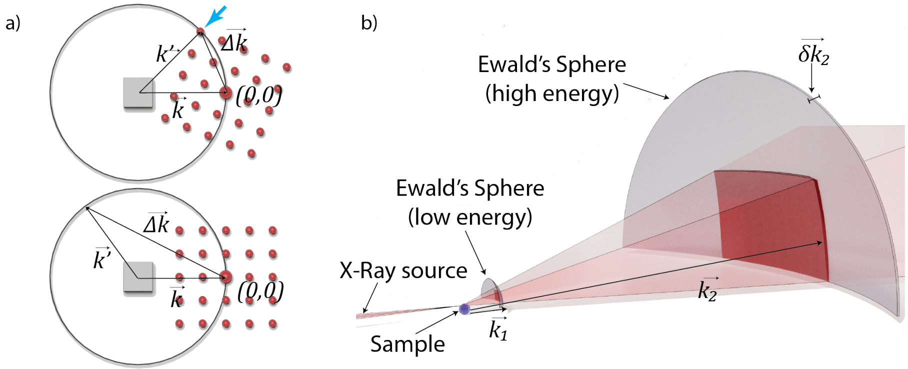

Figure 3.6: *a) 2D representation of the Ewald's sphere's azimuthal rotation around the reciprocal space origin (0,0) for two different orientations. The visible reflection is highlighted by a blue arrow. b) Projection in the lab frame of reference for low* ($\overrightarrow{k_1}$) *and high* ($\overrightarrow{k_2}$) *energy x-rays on 2D detectors with the Ewald sphere thickness given by* $\overrightarrow{\delta k_2}$

Bragg Reflections and Crystal Truncation Rods

As previously mentioned, diffraction is based on the bijective relationship between real ($\mathbb{R}$-space) and reciprocal space ($\mathbb{K}$-space), and it can be demonstrated [54] that this relationship is described by a Fourier transformation, such as:

$$\mathbb{R} \underset{f'}{\overset{f}{\rightleftharpoons}} \mathbb{K} \tag{3.16}$$

$$\begin{aligned} f(x) &= \int_{-\infty}^{\infty} f(x) e^{2\pi i x \xi}\, d\xi \\ f'(\xi) &= \int_{-\infty}^{\infty} f(x) e^{2\pi i x \xi}\, dx \end{aligned} \tag{3.17}$$

Where x is the distance in real space, while ξ represents the spacing in frequency domain, or reciprocal space. The conventional unit for XRD reciprocal space measurements will then be [Å^{-1}].

From the Fourier transform properties, in 3.17, we can mathematically derive how the diffraction pattern generated from an infinite 3D lattice will produce an infinite collection of infinitesimally sharp Bragg reflections in reciprocal space, as can be seen schematically in fig. 3.7.

Application of the same procedure on a finite crystal will consequently result in broadened Bragg reflection, with the size in reciprocal space correlating to the size in real space.

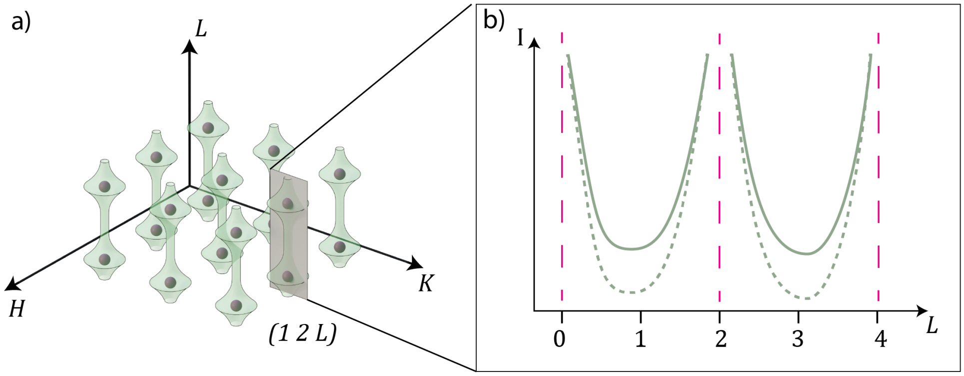

Figure 3.7: *a) schematic visualization of 3D reciprocal space. Bragg reflections are highlighted as red spheres while the green vertical cylinders represent the intensity of the CTRs. b) An example of a (12L) CTR profile is plotted as Intensity vs L-value. Bragg reflections have been arbitrarily put at L=2 and L=4. As a consequence, positions L=1 and L=3 corresponds to Anti-Bragg positions. These are the points in which a maximum change in signal intensity occurs when the surface, and so the CTR in green, undergoes a structural change.*

Consequently, the analysis of the peak shape will then yield the lower limit for the size of crystallites that generated the reflection in the analyzed direction. This is presented in the simple formula:

$$D = \frac{2\pi}{\Delta Q \cdot a_x} \tag{3.18}$$

Where D is the real dimension, ΔQ is the Full With Half Maximum (FWHM) of the reciprocal space feature, and a_x is the lattice dimension of the feature of interest in the specific momentum transfer direction.

If we extend this approach to its extreme such as for semi-2D structures, for instance, thin oxides or surface reconstructions, the reciprocal space signal will result in a line feature. These signals are then called *Crystal Truncation Rods* (CTRs) [74] in case of a truncated surface or, in the case of a thin oxide, *Superstructure Rods.*

In fig. 3.7 presents a schematic view of CTRs (green columns) along with Bragg spots (red spheres) positions. Fig. 3.7a) shows a 2D section representing the rod intensity in the L direction, with oversaturated Bragg reflections at L=0, L=2, and L=4. For reference, in fig. 3.7b) two examples of CTR profiles are shown: full line, with higher intensity, for the case of a smooth surface, while the low intensity profile represents a rough surface. In this representation, the most sensitive positions to surface morphology

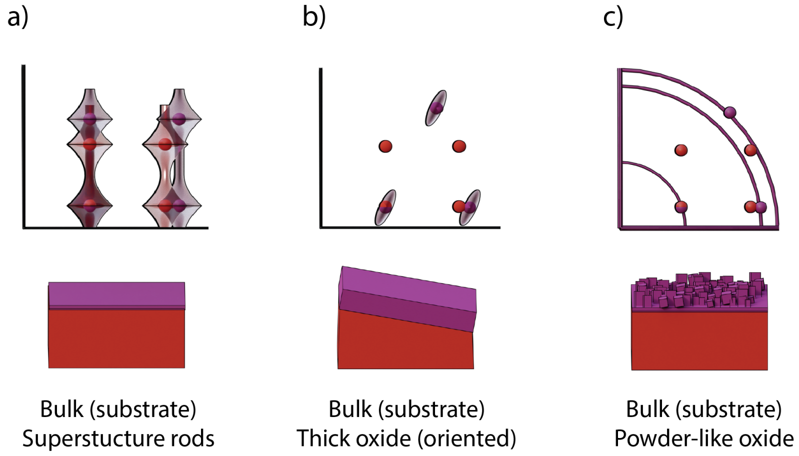

Figure 3.8: *Schematic representation of reciprocal space signal and 3D model for a) superstructure rods for an epitaxial thin film b) Bragg peaks for a film slightly misaligned on z-axis c) Diffraction spheres (more commonly known as rings for 2D detectors) for powder distribution.*

are at L=1 and L=3, and are called *Anti Bragg positions*.

Single and Poly- Crystals vs Powder in diffraction

Above the ideal case of a semi-infinite, single crystal is presented.

For a poly-crystalline or powder sample, a set of Bragg spots will appear for every individual crystallite domain orientation in the sample. Specifically, the intensity of the spots will be correlated, among other things, to the orientation statistics of the original ensemble.

That means that, for a poly-crystalline sample, where the epitaxial orientation marginally deviates from a single crystal, we will have a set of Bragg spots smeared out perpendicular to the crystallites' most common rotational axis, as can be schematically seen in fig. 3.8 b).

For powders, where the orientation is completely random, the Bragg spots will for an homogeneous distribution result in concentric spheres in reciprocal space, centred around spot $(0, 0, 0)$, as from fig. 3.8 c). If we project these spheres on a 2D detector, or line detector, as a function of the diffraction angle Θ, they will be recorded as the more common powder rings or powder diffraction line profiles, respectively.

Ultimately, independently of the data set, we can apply the Rietveld refinement [73] to analyse the phase and size distribution of the sample.

3.3.2 High-Energy Surface X-ray Diffraction and Transmission Surface Diffraction

As mentioned in section 3.1 for all materials there exists a Θ_c angle below which the incoming x-ray light get almost totally externally reflected and the penetration depth is severely limited. By limiting the x-ray penetration depth this phenomenon can consequently enhance significantly the surface sensitivity of techniques such as XRD. This approach is commonly referred as Surface X-ray Diffraction (SXRD) [75]. In SXRD experiments then the signal from CTRs and surface reconstructions is amplified with respect to the bulk Bragg reflections gaining more detailed information on the surface compared to other diffraction geometries.

This work has employed a high energy SXRD variant called High Energy Surface X-ray Diffraction (HEXSRD), which further improves on SXRD. The high energy employed, ranging between 60 and 80 keV compared to the conventional energies of 10 to 30 keV, greatly expands the volume of the Ewald's sphere due to due to high $\vec{k}$, as can be seen from fig. 3.6b). This has the main advantage of drastically reducing the data acquisition time, or alternatively, allowing the acquisition on high throughput time-resolved experiments.

Moreover, the combination of high energy x-rays and grazing incidence geometry means that in the data analysis not only the surface sensitivity will be enhanced, but also that the out-of-plane direction of reciprocal space $\Delta k_\perp$ will be aligned with the z-axis of the reference lab frame. This, combined with the almost negligible curvature of the reciprocal space with respect to the 2D detector, will result in a more intuitive real-time visualization of the data if compared with conventional energies XRD.

Combined with high brilliance sources and large area 2D detectors, HESXRD has proven extremely effective for time resolved [14, 15, 76] as well as detailed fundamental studies [14, 77, 78] of complex sample surfaces in both *in-situ* and *operando* conditions. In this work it has been employed in **paper I** and **III** to generate high frequency, time resolved XRD data following oxidation processes. On **paper VII** it has shown its capabilities not only in time-resolved experiments, but also aquiring a great deal of structural information in a remarkably short amount of time.

Another variation on XRD experimental geometry, and only recently feasible due to a combination of the characteristic high penetration depth of hard x-rays with the very high photon flux and high sensitivity of recent detectors, is the use of transmission geometry XRD. Using this, and fol-

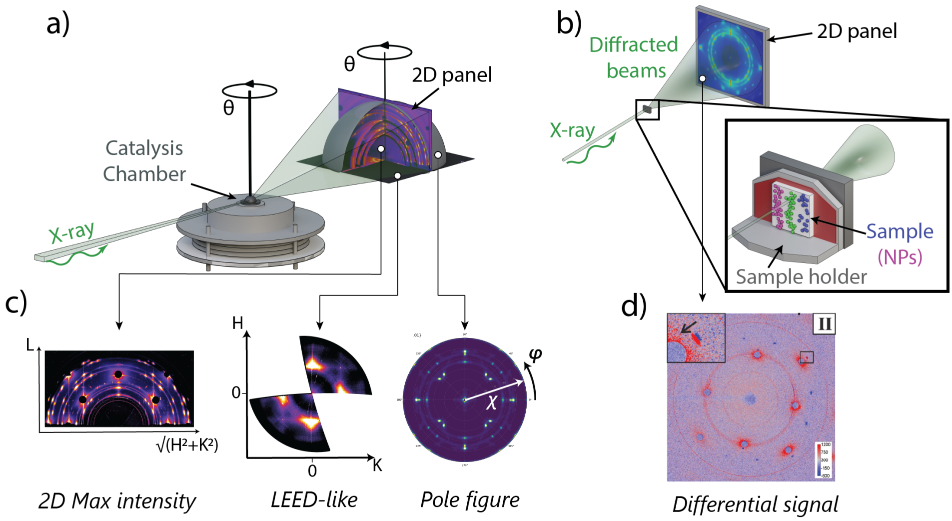

Figure 3.9: *a) Schematic visualization of acquisition for HESXRD. On the left the catalytic chamber, on the right a visualization of the 3D reciprocal space acquired by a rotation along Θ b) TSD set-up with inset showing the sample holder used in* ***paper VI****. c) The different representations used for the HESXRD data. d) Example of the TSD differential signal taken from* ***paper VI****.*

lowing previous works [79, 80], we have demonstrated in **paper VI** that, given a careful subtraction of previous frames, it is possible to follow oxide formation in x-ray Surface Transmission Geometry (TSD) maintaining high structural resolution.

Simplified schematics for both HESXRD and TSD setups are shown in fig. 3.9a-b).

HESXRD data visualization

In this work two main acquisition procedures are implemented. The first is time resolved acquisition, which using fixed sample orientation permits to perform *operando* studies generating high frequency 2D diffraction frames. These data are usually analysed without further reconstruction focusing on crystallographic considerations. This approach has been used because, as presented in previous sections, the minimal correction that would be needed to transform the high $\vec{k}$ spherical projection of the Ewald's sphere onto the 2D detector. These type of data has been extensively used on **paper III, I** and in minor part on **paper VII**.

The second and more complicated acquisition procedure is a rotational scan, which individual frames are integrated in 3D recirpocal-space dataset, as shown in fig. 3.9a). This in turn allows great variety and flexibility in the subsequent data analysis.

There are three possibilities of plotting HESXRD datasets obtained from rotational scans. The first is just to sum them in order to maximize the signal from every individual pixel. The 3D information is lost, but we acquire a fast and comprehensive overview of the sample.

The other two methods are used in order to retrieve the epitaxial nature of the structures present using 3D datasets. In this, the second method projects the 3D reconstructed data into the HK-plane, in a LEED-like fashion, as shown in 3.9c). This representation will have a cartesian coordinates with the in-plane along H and K, while the out of plane along L. This view onto the HK-plane, from the top, integrates the spot intensities over a L-interval, highlighting ROD and CTRs and overall reducing Bragg peak signals.

Third method, to better visualize spots against CTRs/RODs, is the generation of polar plots from 3D datasets. These corresponds to signals integrated over an hemispherical slice of given thickness around relevant Q values. These plots will be then plotted with a view from the top, but their coordinate system will be spherical, with φ as rotational axis along the corresponding L axis, and χ around the X axis.

Finally, for both LEED-like and polar plots, we can integrate the data based on the crystal symmetry of the analysed systems.

3.4 X-Ray Reflectivity

Used as a complementary method, X-ray Reflectivity (XRR) is a technique that takes advantage of the short wavelengths in the x-ray regime in order to generate interference fringes based on the classical Fresnel case of layered multi-material samples [54, 81].

The angular range of the technique is based on the energy used, but usually lies between 0 and 10° for conventional x-rays energies of $\sim$ 10 keV, and between 0 and 1° for high energy x-rays of $\sim$ 70-80 keV.

To infer the structure of the material, the experimental interference curve, shown in fig. 3.10c), is evaluated against a simulated one, generated by an electron density distribution function, exemplified in fig. 3.10b). This is in turn extrapolated from a guess model featuring different layers, in fig. 3.10a). The simulated curve is then made to converge, with a self-consistent procedure, to obtain the best fit between the experimental and

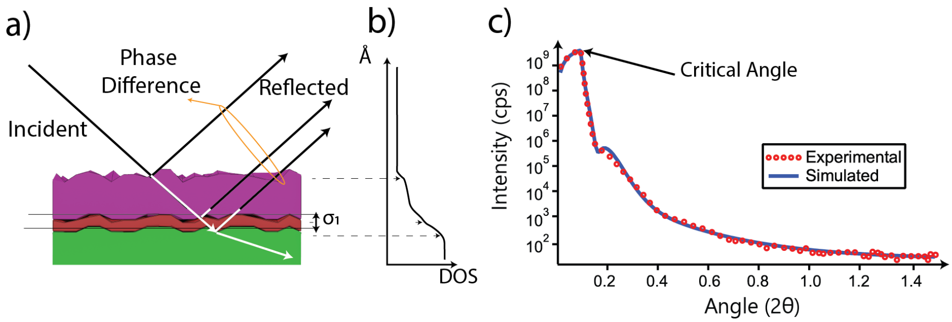

Figure 3.10: *a) Schematic representation for sample comprised of a substrate (green) with two generic layers on top (red-pink). On the left, incident light (x-rays) and on the right both reflected and refracted light is indicated. At the bottom σ_1 refers to the substrate roughness. b) Representation of the electron density perpendicular to the sample surface similar to what would be generated for model fitting c) Example of an XRR measurement, with experimental results and simulation indicated by blue line and red circles respectively, taken from* ***Paper I****.*

the calculated model [82]. At the end of the procedure, several parameters are available such as material coverage, overall interfacial roughness, and thickness of every layer present in the system.

We used XRR as calibration tool for deposition parameters for Rh in **paper VI**, while we used it as supporting technique to HESXRD in **paper VII**.

3.5 Ambient Pressure X-ray Photoelectron Spectroscopy

X-ray Photoelectron Spectroscopy (XPS) is the main spectroscopic technique used in this work. As the name implies, it is a spectroscopic technique that, using photoelectric effect acquires surface sensitive atomic chemical information by analysing the kinetic energy (E_k) of the generated outcoming photoelectrons.

The phenomenon upon which is based is the photoelectric effect, discovered in 1887 and by which explanation Einstein was awarded the Nobel prize in 1906 [83], is the excitation process by which electrons in the target material are excited to the vacuum level and consequently emitted by high energy EM irradiation.

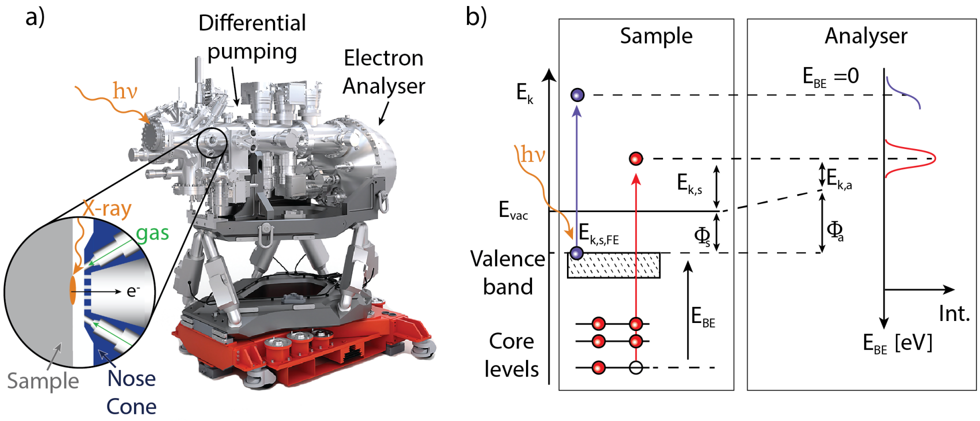

Figure 3.11: *a) Rendering of POLARIS end station at beamline P22, DESY, Germany. Inset shows the close-up cross-section of nose cone for the endstation analyser. [84] b) Energy diagram for core-electron photoemission process.*

The photoemission process, schematically visualized for a core-electron in 3.11b), can be generally expressed by using the energy conservation law, as:

$$E_{BE} = h\nu - E_k - \phi_s \tag{3.19}$$

Where the binding energy E_{BE} equals the photon energy $h\nu$ minus kinetic energy E_k and sample *work function* ϕ_s At this point it has to be differentiated between the sample (s) and analyser (a) frame of reference:

$$E_{k,s} + \phi_s = E_{k,a} + \phi_a \tag{3.20}$$

Furthermore, since the photoelectrons from the *Fermi edge* have $E_{BE} = 0$ by definition, we can write $\phi_a = E_{k,a,FE}$. Re-writing 3.19 in 3.20 we get:

$$E_{BE} = h\nu - E_{k,a} - E_{k,a,FE} \tag{3.21}$$

so the the binding energy E_{BE} is obtained by the difference between photon energy $h\nu$ and measured photoelectron energy $E_{k,a}$ minus a correction term $E_{k,a,FE}$.

From this follow a few important considerations.

Although this process is possible for all electrons in the material, since we want to acquire atomical information in a chemically reactive environment,

---

[2] It has been chosen the energy of 4065 eV as example because it is the mean E_k for Pd3d core-level photoelectrons for POLARIS experiments

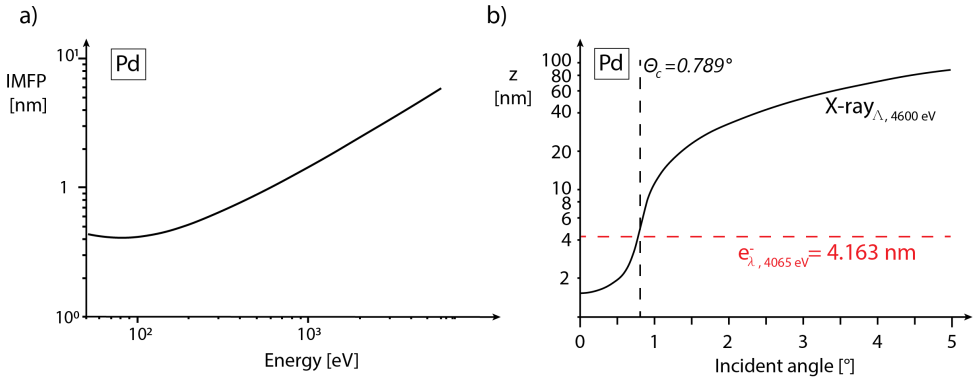

Figure 3.12: *a) Calculated energy dependent IMFP for Pd [85] b) Comparison of angle dependent x-ray penetration depth and IMFP for POLARIS HAXPES experimental conditions* [2]*.*

we need to photo-emit core-electrons. Because of this, given typical core-electron E_{BE} from few tens to few thousands eV, we require radiation in the x-ray energy range, hence the use XPS. The chemical information will be provided through the so called *chemical shift* of the core-electron E_{BE}. This energy shift in core-level E_{BE} is connected to the variation in electron coordination of the valence electrons, that as mentioned in sec. 2.1.1 and 1.1.2, are connected to a number of relevant chemical and physical processes such as oxidation/reduction, physi/chemi-sorption at the surface as well as surface reconstruction.

Once generated, the electrons have to travel to the analyser. It is important to note however, that the electron scattering cross-section is much larger compared to photons, so that the Inelastic Mean Free Path (IMFP [3]) [85] severely limits the electron travel through matter. This electron scattering process usually is the limiting factor for probing depth of XPS signal in the sample as well as limiting factor for environmental pressure surrounding the sample itself.

One way to improve the IMFP [85], is to increase the kinetic energy of the electrons which energy dependence is shown in fig. 3.12. Consequently, and according to eq. 3.19, the E_k can be increased using higher incident energy radiation.

From the experimental point of view the considerations on the limited IMFP explain why XPS is originally used as an Ultra High Vacuum (UHV)

---

[3] Inelastic Mean Free Path (λ) is defined as the distance an electron beam can travel before its intensity decays to $^1/_e$ respect to the original intensity I_0.

technique, so to limit the electron scattering with gas molecules. Throughout the years though, with improvements such as differential stage pumping for gasses and short distances between pumping stages and the sample, XPS setups have been improved to be performed at gradually higher and higher pressures [86]. These high pressure variants then can take several names such as High Pressure XPS (HPXPS) or Ambient Pressure XPS (APXPS), but all presenting similar approaches/results from the experimental point of view.

Another possible variation on the technique, called HArd Xray PhotoEmission Spectroscopy (HAXPES) uses high energy x-rays to increase E_k and IMFP, so to reduce the electrons scattering cross-section with gas molecules and enhance the over signal for higher gas pressures. The drawbacks of this approach though, for surface science community in particular, is the decrease in surface sensitivity due to the higher electron escaping depth from the bulk of the sample as well as the lower photo-ionization cross-section of materials for higher energies.

To counterbalance these disadvantages for hard x-rays the experiments can be performed in Grazing Incident geometry (GI-XPS [87]), to take advantage of the evanescent field interaction as explained in sec. 3.1. With x-ray incident angle $\alpha << \Theta_c$, the x-ray penetration depth decreases such that this process now represents the bottle-neck for electron generation in the sample, as illustrated in fig. 3.2b). The altered penetration depth, integrated in a so called effective IMFP (λ_{eff}), will result in $\lambda_{eff} < \lambda$ and so to enhance surface-to-bulk signal in GI-HAXPES [87, 88] compare to higher incident angles.

In this work we present APXPS results, with x-ray energies between 250 and 720 eV and $\alpha << \Theta_c$, acquired at beamline 23-ID-2 in NSLS-II, Brookhaven, NY. Here we follow IrO_2 titration via CH_4 in **paper IX** and performed HRCLS on Ir/IrO_2 system in **paper VIII**.

HAXPES experiments, at 4600 eV and $\alpha < \Theta_c$, are performed at the POLARIS endstation at P22 beamline at DESY which results are presented in **papers II, IV** and **V**. As aforementioned, a grazing incidence setup is used to achieve high surface sensitivity using hard x-rays. At the same time, due to an innovating design of the nozzle for the electron analyser, shown in inset of fig. 3.11a), we acquire at pressures significantly higher than what has been previously achieved, and up to 1 bar of total pressure.

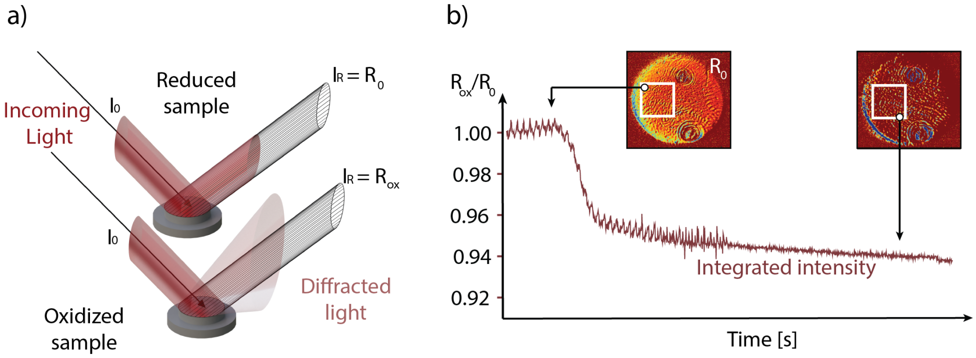

Figure 3.13: *a) Surface Optical Reflectance schematic setup. On top is shown the reflection from metallic (smooth) sample. On the bottom the case of scattered light, typical from oxidized (rough) sample. b) Example of 2D-SOR data over time, taken from* ***Paper I****, with insets showing both the raw images and the ROIs from which the plotted signal is integrated.*

3.6 2D Surface Optical Reflectance

The 2D Surface Optical Reflectance (2D-SOR) presented in this work can be considered a natural evolution, utilizing a 2D detector [16, 89, 90], of the well established industrial point-source reflection spectroscopy [91].

As shown in fig 3.13a), 2D-SOR uses LED light scattered from the sample to probe the change in surface reflectance during, for instance, a catalytic oxidation. The change in reflectance depends either on a change of the material optical properties due to oxidation or other reactions at the surface, or on a change of the surface roughness.

The disentanglement of the various components can be difficult due to the inherent morphological modification due to the chemical reaction at the interface. Nonetheless, the technique is relatively low-cost, simple, and easy to implement on many experimental setup. For these reasons it can be used as a complementary technique, or after being externally validated on a system, used it as main.

Using light in the visible spectrum, 2D-SOR can be used in vacuum, ambient pressure [92] or in liquids [93] regardless and therefore also presents itself as a useful *in-situ* and *operando* technique.

Generally the change of intensity of the signal, usually integrated over a region of interest as shown in fig. 3.13b), is reported such as:

$$\Delta R = \frac{(R_{ox} - R_0)}{R_0} \tag{3.22}$$

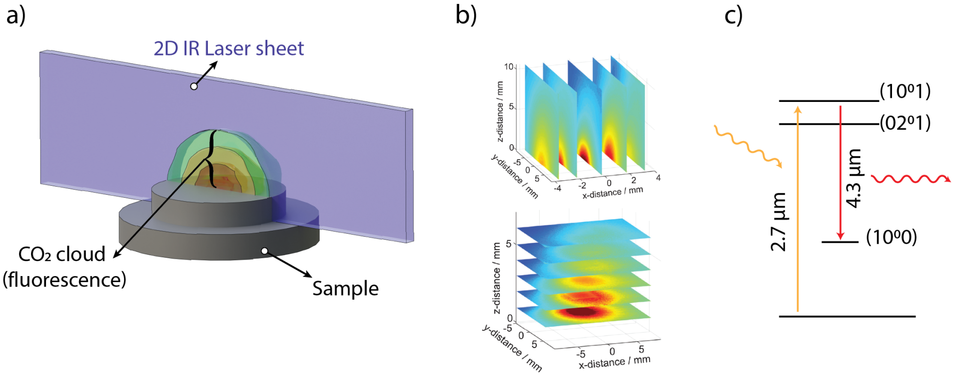

Figure 3.14: *a) Close-up schematic representation of PLIF setup, showing the typical* CO_2 *cloud over an active CO-oxidation catalyst. b) example of systematic use of PLIF to visualize and reconstruct the gas volume, as presented in [95]. c) fluorescence transition for* CO_2 *[96]. Incoming radiation at 2.7* μ*m excites electrons from the ground to the* (10^01) *state to de-excite to* (10^00) *emitting a photon at 4.3* μ*m.*

Where the signal ΔR is a relative quantity, based on the clean sample R_0, so that the nature of the sample is not of relevance. In addition to this, recent improvements to its 2D resolution have brought the resolving power to a few μm^2, so that polycrystalline samples such as foils or industrial-grade steel could be studied under operating conditions [92].

In **paper I** and **III** the method has been combined and compared with HESXRD and PLIF. In particular, we show in **paper I** that the formation of a surface oxide only 2-3 Å thick corresponds to a decrease of the reflectance of around 0.5%, potentially opening the possibility to identify the formation of the surface oxide by 2D-SOR.

3.7 Planar Laser Induced Fluorescence

Planar Induced Fluorescence (PLIF) is a 2D IR laser spectroscopy technique that, using the fluorescence from the de-excitation of pumped molecular rota-vibrational states, probes the concentration of a target gas species in 2-3D fashion [94, 95].

The base phenomenon of *fluorescence* is a *photon absorption-emission* phenomenon. The absorbed light, with λ_a and energy E_a, promotes the transition of electrons between two specific *ground* and *excited* states of the target molecule, with transition specifically occurring only for non-zero changes in a dipole moment [54]. After a characteristic lifetime, in which typically a non-radiant de-excitation occurs, a fluorescence photon is re-emitted at $E_e < E_a$ and corresponding $\lambda_e > \lambda_e$. The intensity of the signal can be expressed as:

$$I_{PLIF} = \eta_c E g f_{(T)} \sigma_0 \chi_{abs} \frac{P}{K_B T} \phi \tag{3.23}$$

Where η_c is the collection efficiency, E is the laser energy, g is the function describing the spectral overlap laser-absorption lineshape, $f_{(T)}$ is the Boltzmann fraction, σ_0 is the absorption cross-section, $\chi_{abs} \frac{P}{K_B} T$ is the number density of the target species and ϕ is the fluorescence quantum yield [97].

While for many molecules of interest such as CO [98], NH_3 [99], NO [100], OH [101] etc., the optimal region is typically in the IR range, the specific excitation wavelength has to be appropriately tuned to avoid spurious signals.

In the case of the rotational-vibrational transition chosen for CO_2 in this thesis, the excitation is at 2.7 μm and the fluorescent signal is at 4.3 μm [102], as shown in 3.14c).

From the experimental point of view, once the laser is properly tuned, the beam can then be shaped by optical elements in a quasi-2D sheet. The fluorescent signal generated will be recorded on a 2D IR detector at a perpendicular angle with respect to the excitation source, as schematically seen in fig. 3.14a). This will produce a single cross-section image of the gas profile in the *Region Of Interest* (ROI). Reshaping the laser and/or moving the sample across the beam will provide a 3D representation, similarly to what presented in fig. 3.14b).

Moreover it is important to note that the laser source must undergo careful and frequent calibration due to several relevant experimental variables affecting measurements such as temperature, pressure, and laser-instability. For these reasons every measurement must include an associate background to yield meaningful data.

PLIF measurements are included in **paper III** to cross-validate the HESXRD and 2D-SOR data about the reactivity/morphology correlation in the PdO/Pd(100) system.

3.8 Density Functional Theory

Density Functional Theory (DFT) is a computational method to calculate the most stable configuration of a given atomic system. At the very core of the method, there are the quantum-mechanical calculations that consist in solving, in approximate form, of the Schrödinger equation for every given atomic arrangement.

The DFT algorithm then iterates these self-consistent calculations, from an initial guess configuration, over several possible other configurations. The algorithm allows the electronic system to relax with each step, adjusting the overall energy landscape and correlated atomic positions until convergence is reached.

This method, although having powerful prediction/explanatory power, represents rather computationally cumbersome tasks. For this reason, while applying the technique, a reasonable sample boundary, optimization methods, and potentially use of cluster computing is advised.

Note that, although present in **paper IX** and **paper VIII**, the calculations were not personally performed and this section is meant only as short introduction to the topic. For further details on theory and applications, please refer to [103, 104]

4. Summary of Papers

This work has been focused on *in-situ* and *operando* multi-technique approach of catalytic surfaces under various catalytic conditions.

Depending on the point of interest, a different line of inquiry can be separated. On the material side, we can distinguish between Pd **paper I, II, III,V, and VIII**; Ir in **paper VII, VIII and IX** while Rh on **paper VI**. On the technique point of view, XRD techniques are used in **paper I, III, VI** and **VII** while XPS is employed in **paper II** and in **paper IV, V, VIII** and **IX** .

Paper I: Surface optical reflectance combined with x-ray techniques during gas-surface interaction

In this report, the change of the 2D-SOR signal has been correlated to the change in the HESXRD signal. The chosen experiment was the oxidation of the Pd(100) surface, in 37 mbar of O_2 partial pressure with 370 mbar total pressure. The experiment has been carried out at the P07 beamline, DESY, Hamburg.

Simultaneous *in-situ* and *operando* HESXRD and 2D-SOR have been performed over a clean Pd(100) during oxidation/reduction cycle to estimate the sensitivity of 2D-SOR as the sample is oxidized. Moreover, after the initial oxidation and before reduction, an XRR measurement was recorded to confirm the HESXRD measurements concerning the oxide thickness. The gas-phase composition was recorded using a mass-spectrometer (MS) throughout the experiment. The slightly different sensitivity has been observed between HESXRD and the 2D-SOR to the two surface oxidation/reduction phenomena has been attributed to a difference in surface roughening behavior, the sensitivity of the 2D-SOR could be shown to be at least in the 2-3 Å range.

Paper II: CO oxidation under lean conditions over Pd(100) model catalyst studied by photoelectron spectroscopy at total pressure of 0.5 bar: closing the gap

This work presents HPXPS results of CO oxidation over Pd(100) at POLARIS endstation at P22 beamline in PETRA III. A total of three pressures up to 500 mbar and two stoichiometric conditions are probed.

The experiments were performed during a heating-cooling ramps in constant pressure and stoichiometric conditions. The high temporal resolution allows to follow *operando* the reaction on Pd and the results show similar CO_2 production with both metallic and oxidized surface, further supporting prior finding concerning the similar catalytic activity of metallic Pd and PdO. After finding the ignition and extinction temperatures we also noted that in all experiments the thermal hysteresis is quite limited, suggesting a less pronounced by-stability effect at higher pressures compared to that previously observed at lower and UHV pressures. Finally, we also calculate the activation energy for the two stoichiometric ratios with values that differs from the previously tabulated one at UHV as well as at high pressure but different stoichiometry. We argue that this might be connected to the nature of the gas mixture and that the pressure seems to play only a minor role for determining the activation energy of this specific reaction conditions but further investigation are needed.

Paper III: Combining High-energy x-ray Diffraction with Surface Optical Reflectance and Planar Laser Induced Fluorescence for operando catalyst surface characterization

In this contribution, a combination of the *in-situ* techniques: HESXRD, 2D-SOR, MS, and PLIF is used to study the CO oxidation over Pd(100), using a total pressure of 180 mbar and various O_2:CO_2 ratios. The experiment was performed at the P07 beamline, DESY, Hamburg.

The synchronization of the techniques has been implemented using a trigger from the beamline. After the initial triggering, both PLIF and SOR were synchronized at a 10 Hz acquisition rate, while HESRXD and MS were ∼2 Hz. Through 2D-SOR images from the surface, the inhomogeneity of the sample during oxidizing conditions could be confirmed and correlated to the CO_2 gas phase distribution above the sample measured by PLIF.

The measurements show that the direct gas-phase measurements by PLIF have a noticeable time-resolution advantage compared to MS. This, in turn, shows the need for as delay-free as possible investigation methods when dealing with *operando* measurements.

Paper IV: Bridging the pressure gap in CO oxidation

This contribution presents the HPXPS results for CO oxidation over Pd(100) model catalyst, obtained up at 1 bar of total pressure, with the POLARIS endstation at beamline P22 in PETRA III, DESY, Hamburg.

The reaction of CO oxidation is performed at 1:1 $CO:O_2$ ratio and O_2 partial pressure up to 100 mbar with He as filling gas. The temperature range between 50 and 480 °C, with the 1 bar experiment between 360 and 480 °C.

The results show, with remarkably high-quality data, that the barrier activation energy of CO oxidation at high pressure is comparable to the literature data for lower pressures, so beginning to bridge the *pressure gap* between model and industrial catalytic reactions.

Paper V: The Structure of the Active Pd state During Catalytic CO oxidization

This paper presents the angle-dependent HPXPS results from CO oxidation and reduction on PdO/Pd(100) system with the POLARIS endstation, beamline P22 in PETRA III, DESY, Hamburg.

The reaction of CO oxidation was performed on Pd(100), at a 50:4 O_2:CO ratio, 300 mbar of pressure, and a temperature between 200 and 450 °C. Initial the sample is oxidized to bulk PdO(101) at high temperature. During the descending temperature ramp, the reduction phase is halted. An angle dependant HPXPS series of spectra were taken under reaction conditions to investigate the reduction mechanism of the newly formed PdO.

The results, combined with a modeling of the proposed reduction mechanism, show that a multilayer system is formed with metallic islands growing on top of the reducing oxide during reduction.

Paper VI: Transmission Surface Diffraction applied to model catalyst surfaces during catalytic gas-surface interactions

The paper presents the results of the novel developed for Transmission Surface Diffraction (TSD) from *operando* oxidation on Rh film as well as Rh nanoparticles (NPs) deposited on MgO substrate.

The experiments were performed at beamline ID31, ESRF at 70 keV and at beamline P07, DESY at 79.5 keV.

The films were tested under 1 bar of total pressure, with alternating reducing and oxidizing conditions and at constant 700 K. In these conditions it was possible to follow formation of Rh_2O_3 with a 10 min time resolution.

Rocking scans were performed around (200) Rh Bragg spot to test the resolution and accuracy of TSD. It was possible to distinguish and reconstruct in the 3D reciprocal space the characteristic star patterned metallic CTRs passing by the (200) spot.

The results show that with the current setup, it is possible to follow the oxidation on top of both film and metallic nanoparticles. The current method presents multiple advantages compared to the traditional XRD technique and could represent an interesting tool for the surface science community with further development.

Paper VII: Oxidation and reduction of Ir(100) studied by High Energy Surface X-Rays Diffraction

The paper focused on the structural determination of Ir/IrO_2 during red/ox reaction of the surface at 775 K and 500 mbar of total pressure and under 3 different O_2 partial pressures such as 2.5, 5, and 10 mbar. The *in-situ* and *operando* measurements were carried out at beamline P07, DESY, Hamburg.

The results show gradual evolution from oxygen adsorption, through onset of different phases, to the dynamical equilibrium of multiple oxide factes on the surface. Specifically for the 2.5 mbar O_2 condition a coexistence of c(2x2) Ir(100)-O, to our knowledge never observed before, and IrO_2(110) is present whaeter at higher O_2 partial pressures a mixture of IrO_2(101), IrO_2(110) and IrO_2(100) is present.

Upon reduction with CO, the formation of metastable Ir(111) facets and/or vicinal Ir(221) surfaces are observed. This metallic island formation on top of the oxide layer, similar to what is observed for the Pd case, could be the insight in yet unknown catalysis behaviour with future implications for dynamic metal-oxide systems.

Paper VIII: High-Resolution x-ray Photoelectron Spectroscopy of an $IrO_2(110)$ Film on Ir(100)

This paper presents results from high-resolution XPS data, combined with DFT calculation, on the thermal oxidation of Ir(100)/$IrO_2(110)$.

After thermal oxidation of Ir(100), at 3 Torr and 775 K for 10 min, high-resolution Ir4f, O1s spectra are gathered to chemically investigate the $IrO_2(110)$ surface structure. After oxidation and spectra are taken at a high temperature (600 K), the sample is let cool down. For both cases, high-resolution spectra are taken, and the surface and bulk components are identified. Furthermore, upon cool down, it is noted that surface terminal oxygens (O_{ot}) in the bulk oxide is reduced to hydroxyl groups, attributed to reaction with residual H_2 or H_2O in the chamber.

For all the observations mentioned above, DFT calculations have been provided as validation methods for our findings.

Paper IX: Isothermal Reduction of IrO_2 (110) Films by Methane Investigated Using In-Situ x-ray Photoelectron Spectroscopy

This contribution investigates the titration of $IrO_2(110)$ via CH_4, investigated with both DFT theoretical method and *in-situ* XPS; performed at the beamline 23-ID-2 at National Synchrotron Light Source II, Brookhaven, New York.

The IrO_2 oxide films are prepared by Ir(100) thermal oxidation in 3 Torr of O_2 at a temperature of 775 K for 10 min. The films are then isothermally reduced in 10^{-5} Torr of CH_4 for 50 min or until the extensive reduction of the surface. During the whole experiments, Ir4f, C1s and O1s core-level spectra were continually collected to form a trend for temperatures from 500 K to 650 K, at 50 K intervals.

Theoretical DFT calculations were used to support the experimental finding.

Our findings confirm previous observations about the selectivity of CH_4 oxidation for $IrO_2(110)$ compared to metallic Ir. DFT calculations suggest that oxidation of CH_4 in the tested conditions convert O_{br} sites of $IrO_2(110)$

into HO_{br}. At the same time, upon complete reduction of top layer oxide, the subsurface oxygen replenish the top O_{br}. This proceeds until complete titration of the oxide of interest.

5. Conclusion and Outlook

> *"The aim of science is not to open the door to infinite wisdom,*
> *but to set some limit on infinite error."*
> *- Life of Galileo (1939), Bertolt Brecht -*

Catalysis and catalysts represent a fundamental part of modern livelihood nowadays and are likely to grow in importance, similarly to their rise in the 20th century. The study and atomic characterization of heterogeneous catalysts through their model systems and the reactions at surfaces represents the first and essential step in understanding and engineering for the future of the field. With this perspective, it is also fundamental to continuously improve and validate new methods to push the limits of the state-of-the-art and enhance the toolbox available for surface science and catalysis for the future.

This work has presented a number of different light-matter interaction techniques, mainly based on synchrotron radiation methods, to investigate a reaction *in-situ* and *operando*, further closing the material and pressure gap typical for model catalysts studies.

To summarize some of the findings some of the result in this thesis. It has been shown that upon oxidation, the Ir(100) surface do not only exposes the IrO_2(110) surface as previously reported, but also IrO_2(100) and (101) surfaces (**paper VII**). Although this discrepancy may be due to differences in oxidation temperatures or residual gas composition, the results still demonstrate the more complex oxidation behavior of the Ir(100) surface compared to the Pd(100) surface. As a consequence, more well-ordered IrO_2(110) surfaces has been made by using thin IrO_2 films on various rutile (110) surfaces [17].

Another highlight is the observation of the formation of metallic island in the Ir and Pd oxide films studied in reducing conditions (**papers VII** and **V**). Such a metal-oxide mixed system observed on both Pd and Ir could point to a generalization for reduction conditions. This could provide an interesting and dynamic system under reaction conditions for future studies and, in particular, the study of the promoting or poisoning effects could be interesting point of investigation by various methods.

On the technical side, the thesis shows the benefit to use 2D-SOR in combination with grazing incident techniques. In particular, this thesis shows that the 2D-SOR signal is able to detect a flat ultra-thin surface oxide forming on a Pd(100) surface. The limit of the sensitivity is not yet fully explored, and could be an interesting future research topic.

Finally, a new XPS analyser has been used, capable of performing surface sensitive XPS at pressures far beyond what has been previously possible. Our measurements confirm previous observations, and in this way validate the surface sensitivity while using HAXPES in grazing incidence geometry to enhance its surface sensitivity. Although the POLARIS setup is technical demanding, it finally brings XPS to atmospheric conditions and is likely to have a tremendous impact on catalysis related research.

Bibliography

[1] J. Wisniak, *The history of catalysis. from the beginning to nobel prizes*, Educación Química **21** (2010), no. 1, 60 – 69.

[2] P.W.N.M. van Leeuwen J.A. Moulijn and R.A. van Santen, *Studies in surface science and catalysis*, vol. 79, Elsevier, 1993.

[3] Kurt W. Kolasinsky, *Surface science: Foundations of catalysis and nanoscience*, Wiley (2012).

[4] G. Ertl, *Wilhelm Ostwald: Founder of physical chemistry and nobel laureate 1909*, Angew. Chem. Int. Ed. **48** (2009), no. 36, 6600–6606.

[5] F. Haber, *The synthesis of ammonia from its elements Nobel lecture, june 2, 1920*, Resonance **7** (2002), no. 9, 86–94.

[6] C. P. Casey, *2005 nobel prize in chemistry. development of the olefin metathesis method in organic synthesis*, Journal of Chemical Education **83** (2006), no. 2, 192.

[7] W. S. Knowles, *Asymmetric hydrogenations (nobel lecture 2001)*, Advanced Synthesis & Catalysis **345** (2003), no. 1-2, 3–13.

[8] *Nobel prizes 2010: Richard F. Heck, Ei-ichi Negishi, Akira Suzuki*, Angew. Chem. Int. Ed. **49** (2010), no. 45, 8300–8300.

[9] G. Wilke, *Fifty years of Ziegler catalysts: Consequences and development of an invention*, Angew. Chem. Int. Ed. **42** (2003), no. 41, 5000–5008.

[10] S. Gross G.Centi, S. Parathoner and E. J. M. Hensen, *Science and technology roadmap on catalysis for europe: a path to create a sustainable future*, European cluster on catalysis (2016).

[11] Ertl G., *Reactions at solid surfaces*, Wiley, 2010.

[12] K. W. Kolasinsky, *Mind the gap.*, Nat Catal **1** (2018), 807808.

[13] H. J. Freund, H. Kuhlenbeck, J. Libuda, G. Rupprechter, M. Bäumer, and H. Hamann, *Bridging the pressure and materials gaps between catalysis and surface science: clean and modified oxide surfaces*, Top. Catal. **15** (2001), no. 2, 201–209.

[14] M. Shipilin, J. Gustafson, C. Zhang, L. R. Merte, A. Stierle, U. Hejral, U. Ruett, O. Gutowski, M. Skoglundh, P.-A. Carlsson, and E. Lundgren, *Transient structures of PdO during CO oxidation over Pd(100)*, J. Phys. Chem. C **119** (2015), no. 27, 15469–15476.

[15] E. Lundgren, C. Zhang, L. R. Merte, M. Shipilin, S. Blomberg, U. Hejral, J. Zhou, J. Zetterberg, and J. Gustafson, *Novel in situ techniques for studies of model catalysts*, Acc. Chem. Res. **50** (2017), no. 9, 2326–2333, PMID: 28880530.

[16] J. Zhou, S. Blomberg, J. Gustafson, E. Lundgren, and J. Zetterberg, *Simultaneous imaging of gas phase over and surface reflectance of a Pd(100) single crystal during CO oxidation*, J. Phys. Chem. C **121** (2017), no. 42, 23511–23519.

[17] M. J. S. Abb, T. Weber, D. Langsdorf, V. Koller, S. M. Gericke, S. Pfaff, M. Busch, J. Zetterberg, A. Preobrajenski, H. Grönbeck, E. Lundgren, and H. Over, *Thermal stability of single-crystalline IrO_2(110) layers: Spectroscopic and adsorption studies*, J. Phys. Chem. C **124** (2020), no. 28, 15324–15336.

[18] K. Morgan, J. Touitou, J.-S. Choi, C. Coney, C. Hardacre, J. A. Pihl, C. E. Stere, M.-Y. Kim, C. Stewart, A. Goguet, and W. P. Partridge, *Evolution and enabling capabilities of spatially resolved techniques for the characterization of heterogeneously catalyzed reactions*, ACS Catal. **6** (2016), no. 2, 1356–1381.

[19] M. De Graef and M. E. McHenry, *Structure of materials: An introduction to crystallography, diffraction and symmetry*, Cambridge University Press, 2007.

[20] M. Ladd and R. Palmer, *Structure determination by x-ray crystallography: Analysis by x-rays and neutrons*, Springer, 2013.

[21] S.L. Chang and P. A. Thiel, *Oxygen on Pd(100): Order, reconstruction, and desorption*, J. Chem. Phys. **88** (1988), no. 3, 2071–2082.

[22] P. Ferstl, T. Schmitt, M. A. Schneider, L. Hammer, A. Michl, and S. Müller, *Structure and ordering of oxygen on unreconstructed Ir(100)*, Phys. Rev. B **93** (2016), 235406.

[23] K. Anic, A. V. Bukhtiyarov, H. Li, C. Rameshan, and G. Rupprechter, *CO adsorption on reconstructed Ir(100) surfaces from UHV to mbar pressure: A LEED, TPD, and PM-IRAS study*, J. Phys. Chem. C **120** (2016), no. 20, 10838–10848, PMID: 27257467.

[24] Mohammad Alif Arman, Andreas Klein, Pascal Ferstl, Abhilash Valookaran, Johan Gustafson, Karina Schulte, Edvin Lundgren, Klaus Heinz, Alexander Schneider, Florian Mittendorfer, Lutz Hammer, and Jan Knudsen, *Adsorption of hydrogen on stable and metastable ir(100) surfaces*, Surface Science **656** (2017), 66–76.

[25] K. Heinz and L. Hammer, *Nanostructure formation on ir(100)*, Progress in Surface Science **84** (2009), no. 1, 2–17.

[26] Z. Liang, T. Li, M. Kim, A. Asthagiri, and J. F. Weaver, *Low-temperature activation of methane on the* IrO_2*(110) surface*, Science **356** (2017), no. 6335, 299.

[27] Yingxue Bian, Tao Li, and Jason F. Weaver, *Structure and reactivity of iridium oxide layers grown on ir(100) by oxidation at sub-ambient o2 pressures*, Journal of Physics D: Applied Physics **52** (2019), no. 43, 434002.

[28] H. Ibach, *Physics of surfaces and interfaces*, Springer, 2006.

[29] H.-J. Freund, G. Meijer, M. Scheffler, R. Schlögl, and M. Wolf, *CO oxidation as a prototypical reaction for heterogeneous processes*, Angew. Chem. Int. Ed. **50** (2011), no. 43, 10064–10094.

[30] Le Chatelier and O Boudouard, *Limits of flammability of gaseous mixtures*, Bulletin de la Société Chimique de France (1898).

[31] J.W. Niemantsverdriet I. Chorkendorff, *Concepts of modern catalysis and kinetics*, Wiley (2003).

[32] J. Hagen, *Industrial catalysis: A practical approach*, Wiley, 2015.

[33] M. A. van Spronsen, J. W. M. Frenken, and I. M. N. Groot, *Surface science under reaction conditions: CO oxidation on pt and Pd model catalysts*, Chem. Soc. Rev. **46** (2017), 4347–4374.

[34] J. F. Weaver, *Surface chemistry of late transition metal oxides*, Chem. Rev. **113** (2013), no. 6, 4164–4215, PMID: 23414244.

[35] H. Over, *Surface chemistry of ruthenium dioxide in heterogeneous catalysis and electrocatalysis: From fundamental to applied research*, Chem. Rev. **112** (2012), no. 6, 3356–3426, PMID: 22423981.

[36] J. F. Weaver, J. Choi, V. Mehar, and C. Wu, *Kinetic coupling among metal and oxide phases during CO oxidation on partially reduced PdO(101): Influence of gas-phase composition*, ACS Catal. **7** (2017), no. 10, 7319–7331.

[37] Y. Bian, M. Kim, T. Li, A. Asthagiri, and J. F. Weaver, *Facile dehydrogenation of ethane on the* IrO_2*(110) surface*, J. Am. Chem. Soc. **140** (2018), no. 7, 2665–2672, PMID: 29376362.

[38] H. Over, Y. D. Kim, A. P. Seitsonen, S. Wendt, E. Lundgren, M. Schmid, P. Varga, A. Morgante, and G. Ertl, *Atomic-scale structure and catalytic reactivity of the* RuO_2*(110) surface*, Science **287** (2000), no. 5457, 1474–1476.

[39] R. J. Farrauto, M. Deeba, and S. Alerasool, *Gasoline automobile catalysis and its historical journey to cleaner air*, Nat. Cat. **2** (2019), no. 7, 603–613.

[40] Feng Gao, Sean M. McClure, Y. Cai, Kerrie K. Gath, Yilin Wang, Mingshu Chen, Q. Q. Guo, and D. Wayne Goodman, *Co oxidation trends on pt-group metals from ultrahigh vacuum to near atmospheric pressures: A combined in situ pm-iras and reaction kinetics study*, Surface Science **603** (2009), 65–70.

[41] T. Engel and G. Ertl, *Surface residence times and reaction mechanism in the catalytic oxidation of co on pd(111)*, Chemical Physics Letters **54** (1978), no. 1, 95–98.

[42] Willem G. Onderwaater, Olivier Balmes, Sander B. Roobol, Matthijs Van Spronsen, Jakub Drnec, Francesco Carla, Roberto Felici, and Joost W. M. Frenken, *Oxidation of co on pd(1ă0ă0): on*

the structural evolution of the pdo layer during the self sustained oscillation regime, Catalysis, Structure & Reactivity **3** (2017), no. 1-2, 89–94.

[43] Janne T. Hirvi, Toni-Jani J. Kinnunen, Mika Suvanto, Tapani A. Pakkanen, and Jens K. Nørskov, *Co oxidation on pdo surfaces*, The Journal of Chemical Physics **133** (2010), no. 8, 084704.

[44] M. Ravi, M. Ranocchiari, and J. A. van Bokhoven, *The direct catalytic oxidation of methane to methanola critical assessment*, Angew. Chem. Int. Ed. **56** (2017), no. 52, 16464–16483.

[45] P. Weiland, *Biogas production: current state and perspectives*, Applied Microbiology and Biotechnology **85** (2010), no. 4, 849–860.

[46] F. Schüth, *Making more from methane*, Science **363** (2019), no. 6433, 1282–1283.

[47] R. Horn and R. Schlögl, *Methane activation by heterogeneous catalysis*, Cat. Letters **145** (2015), no. 1, 23–39.

[48] J. Wang, Y. Yun, and E.I. Altman, *The plasma oxidation of pd(100)*, Surface Science **601** (2007), no. 16, 3497–3505.

[49] Edvin L.n, Anders M., Jesper N A., Georg K., Michael S., and Peter V., *Surface oxides on close-packed surfaces of late transition metals*, J. Condens. Matter Phys. **18** (2006), no. 30, R481–R499.

[50] Mikhail Shipilin, Andreas Stierle, Lindsay R. Merte, Johan Gustafson, Uta Hejral, Natalia M. Martin, Chu Zhang, Dirk Franz, Volkan Kilic, and Edvin Lundgren, *The influence of incommensurability on the long-range periodicity of the Pd(100)-(5Œ5)R27°-PdO(101)*, Surface Science **660** (2017), 1–8.

[51] R. van Rijn, O. Balmes, A. Resta, D. Wermeille, R. Westerström, J. Gustafson, R. Felici, E. Lundgren, and J. W. M. Frenken, *Surface structure and reactivity of Pd(100) during CO oxidation near ambient pressures*, Phys. Chem. Chem. Phys. **13** (2011), 13167–13171.

[52] J. Gustafson, O. Balmes, C. Zhang, M. Shipilin, A. Schaefer, B. Hagman, L. R. Merte, N. M. Martin, P.-A. Carlsson, M. Jankowski, E. J.

Crumlin, and E. Lundgren, *The role of oxides in catalytic CO oxidation over rhodium and palladium*, ACS Catal. **8** (2018), no. 5, 4438–4445.

[53] A. D. McNaught and A. Wilkinson, *Fundamentals of photonics, 2nd edition*, Wiley, 2007.

[54] D. McMorrow J. A.-Nielsen, *Elements of modern x-ray physics - 2nd ed*, Wiley (2010).

[55] David A. Woods and Colin D. Bain, *Total internal reflection spectroscopy for studying soft matter*, Soft Matter **10** (2014), 1071–1096.

[56] Cesar S. Huertas, Olalla Calvo-Lozano, Arnan Mitchell, and Laura M. Lechuga, *Advanced evanescent-wave optical biosensors for the detection of nucleic acids: An analytic perspective*, Frontiers in Chemistry **7** (2019), 724.

[57] *X-ray server*, `https://x-server.gmca.aps.anl.gov`, 2021.

[58] Sergey A. Stepanov, *X-ray server: an online resource for simulations of x-ray diffraction and scattering*, Advances in Computational Methods for X-Ray and Neutron Optics (Manuel Sanchez del Rio, ed.), vol. 5536, International Society for Optics and Photonics, SPIE, 2004, pp. 16 – 26.

[59] *Gixa - x-ray tools*, `https://gixa.ati.tuwien.ac.at/tools/index.xhtml`, 2021.

[60] B.L. Henke, E.M. Gullikson, and J.C. Davis, *X-ray interactions: Photoabsorption, scattering, transmission, and reflection at e = 50-30,000 ev, z = 1-92*, Atomic Data and Nuclear Data Tables **54** (1993), no. 2, 181–342.

[61] W.W. Van Den Hoogenhof and D.K.G. De Boer, *Glancing-incidence x-ray analysis*, Spectrochimica Acta Part B: Atomic Spectroscopy **48** (1993), no. 2, 277–284.

[62] M. A. Newton, *Operando catalysis using synchrotron methods*, Catal. Struct. React. **3** (2017), no. 1-2, 2–4.

[63] *How does a synchrotron radiation source work?*, `https://photon-science.desy.de/research/students__teaching/primers/synchrotron_radiation/index_eng.html`, 2021.

[64] N. Schell, A. King, F. Beckmann, T. Fischer, M. Müller, and A. Schreyer, *The high energy materials science beamline (HEMS) at PETRA III*, Mechanical Stress Evaluation by Neutrons and Synchrotron Radiation VI, Materials Science Forum, vol. 772, Trans Tech Publications Ltd, 2 2014, pp. 57–61.

[65] P. et al. Amann, *A high-pressure x-ray photoelectron spectroscopy instrument for studies of industrially relevant catalytic reactions at pressures of several bars*, Rev. Sci. Instrum. **90** (2019), no. 10, 103102.

[66] C. Schlueter, A. Gloskovskii, K. Ederer, I. Schostak, S. Piec, I. Sarkar, Yu. Matveyev, P. Lömker, M. Sing, R. Claessen, C. Wiemann, C. M. Schneider, K. Medjanik, G. Schönhense, P. Amann, A. Nilsson, and W. Drube, *The new dedicated HAXPES beamline P22 at PETRA III*, AIP Conf. Proc. **2054** (2019), no. 1, 040010.

[67] C Sánchez-Hanke, S L Hulbert, D Shapiro, and R Reininger, *High coherent flux at the NSLS-II coherent soft x-ray beamline*, J. Phys. Conf. Ser. **425** (2013), no. 15, 152017.

[68] W. Friedrich, P. Knipping, and M. von Laue, *Interferenz-erscheinungen bei röntgenstrahlen*, Mathematisch-Physikalische Klasse: Sitzungsberichte, Verlag der Kgl. Bayer. Akad. der Wiss., 1912.

[69] L. Martiradonna, *A photograph of crystal order*, Nature **511** (2014), no. 7.

[70] O. Epp J. Deisenhofer, R. Huber K. Miki, and H. Michel, *Structure of the protein subunits in the photosynthetic reaction centre of rhodopseudomonas viridis at 3 Å resolution*, Nature (1985), no. 318, 618624.

[71] W.L Bragg, W.H.; Bragg, *The reflection of x-rays by crystals*, Proc. R. Soc. Lond. A (1913), no. 88(605), 428438.

[72] Philip W., *An introduction to synchrotron radiation - techniques and applications*, Wiley (2011).

[73] H. M. Rietveld, *A profile refinement method for nuclear and magnetic structures*, J. Appl. Crystallogr. **2** (1969), no. 2, 65–71.

[74] I. K. Robinson, *Crystal truncation rods and surface roughness*, Phys. Rev. B **33** (1986), 3830–3836.

[75] R. Feidenhans'l, *Surface structure determination by x-ray diffraction*, Surf. Sci. Rep. **10** (1989), no. 3, 105 – 188.

[76] U. Hejral, P. Müller, O. Balmes, D. Pontoni, and A. Stierle, *Tracking the shape-dependent sintering of platinumrhodium model catalysts under operando conditions*, Nat. Commun. **7** (2016), no. 1, 10964.

[77] U. Hejral, P. Müller, M. Shipilin, J. Gustafson, D. Franz, R. Shayduk, U. Rütt, C. Zhang, L. R. Merte, E. Lundgren, V. Vonk, and A. Stierle, *High-energy x-ray diffraction from surfaces and nanoparticles*, Phys. Rev. B **96** (2017), 195433.

[78] J. Gustafson, M. Shipilin, C. Zhang, A. Stierle, U. Hejral, U. Ruett, O. Gutowski, P. A. Carlsson, M. Skoglundh, and E. Lundgren, *High-energy surface x-ray diffraction for fast surface structure determination*, Science **343** (2014), no. 6172, 758.

[79] Hiroo T., Osami S., and Toshio T., *Surface x-ray diffraction in transmission geometry*, Appl. Surf. Sci. **234** (2004), no. 1, 403–408, The Ninth International Conference on the Formation of Semiconductor Interfaces,.

[80] Hiroo T., *Progress in surface x-ray crystallography and the phase problem*, Jpn. J. Appl. Phys. **59** (2020), no. 2, 020503.

[81] D. K. G. de Boer, *X-ray reflection and transmission by rough surfaces*, Phys. Rev. B **51** (1995), 5297–5305.

[82] M. Björck and G. Andersson, *GenX: an extensible X-ray reflectivity refinement program utilizing differential evolution*, J. Appl. Crystallogr. **40** (2007), no. 6, 1174–1178.

[83] A. Chodos and J. Ouellette, *Einstein and the photoelectric effect*, APS **14** (2005), no. 1.

[84] *Scienta-omicron bar xps system*, `https://scientaomicron.com/en/system-solutions/electron-spectroscopy/BAR-XPS`, 2021.

[85] C. J. Powell, *Practical guide for inelastic mean free paths, effective attenuation lengths, mean escape depths, and information depths in x-ray photoelectron spectroscopy*, Journal of Vacuum Science & Technology A **38** (2020), no. 2, 023209.

[86] Hofmann S., *Auger- and x-ray photoelectron spectroscopy in materials science*, Springer, 2013.

[87] W. Drube, A. Lessmann, and G. Materlik, *Xray standing waves and xray photoemission measurements in the energy range 2.77 kev*, Rev. Sci. Instrum. **63** (1992), no. 1, 1138–1141.

[88] Sergey S., *X-ray server: an online resource for simulations of x-ray diffraction and scattering*, Proceedings SPIE **5536** (2004), 16–26.

[89] W. G. Onderwaater, A. Taranovskyy, G. C. van Baarle, J. W. M. Frenken, and I. M. N. Groot, *In situ optical reflectance difference observations of CO oxidation over Pd(100)*, J. Phys. Chem. C **121** (2017), no. 21, 11407–11415.

[90] W. G. Onderwaater, A. Taranovskyy, G. M. Bremmer, G. C. van Baarle, J. W. M. Frenken, and I. M. N. Groot, *From dull to shiny: A novel setup for reflectance difference analysis under catalytic conditions*, Rev. Sci. Instrum. **88** (2017), no. 2, 023704.

[91] Y. Borensztein, *Surface optical reflectance spectroscopies: Application to semiconductor and metal surfaces*, Physica A Stat. Mech. Appl. **207** (1994), no. 1, 293 – 301.

[92] S. Pfaff, A. Larsson, D. Orlov, G. S. Harlow, G. Abbondanza, W. Linpé, L. Rämisch, S. M. Gericke, J. Zetterberg, and E. Lundgren, *Operando reflectance microscopy on polycrystalline surfaces in thermal catalysis, electrocatalysis, and corrosion*, ACS Appl. Mater. Interfaces **13** (2021), no. 16, 19530–19540, PMID: 33870682.

[93] W. Linpé, G. S. Harlow, A. Larsson, G. Abbondanza, L. Rämisch, S. Pfaff, J. Zetterberg, J. Evertsson, and E. Lundgren, *An electrochemical cell for 2-dimensional surface optical reflectance during anodization and cyclic voltammetry*, Rev. Sci. Instrum. **91** (2020), no. 4, 044101.

[94] G. Kychakoff, R. D. Howe, R. K. Hanson, M. C. Drake, R. W. Pitz, M. Lapp, and C. M. Penney, *Visualization of turbulent flame fronts with planar laser-induced fluorescence*, Science **224** (1984), no. 4647, 382–384.

[95] S. Blomberg, J. Zhou, J. Gustafson, J. Zetterberg, and E. Lundgren, *2d and 3d imaging of the gas phase close to an operating model catalyst by planar laser induced fluorescence*, J. Condens. Matter Phys. **28** (2016), 453002.

[96] Z. S. Li, J. Zetterberg, P. Malm, and M. Aldén, *Investigation of* CO_2 *infrared chemiluminescence emission and LIF detection for combustion diagnostics applications*, Proceedings of the European Combustion Meeting (2005).

[97] J. Zetterberg, S. Blomberg, Gustafson, and J. et al, *Spatially and temporally resolved gas distributions around heterogeneous catalysts using infrared planar laser-induced fluorescence*, Nat Commun **6** (2015), no. 7076.

[98] M. Aldén, S. Wallin, and W. Wendt, *Applications of two-photon absorption for detection of CO in combustion gases*, Appl. Phys. B **33** (1984), no. 4, 205–208.

[99] S. Blomberg, Jianfeng Z., J. Gustafson, J. Zetterberg, and E. Lundgren, *2d and 3d imaging of the gas phase close to an operating model catalyst by planar laser induced fluorescence*, IOP Publishing **28** (2016), no. 45, 453002.

[100] A. Zellner, R. Suntz, and O. Deutschmann, *Two-dimensional spatial resolution of concentration profiles in catalytic reactors by planar laser-induced fluorescence: NO reduction over diesel oxidation catalysts*, Angew. Chem. Int. Ed. **54** (2015), no. 9, 2653–2655.

[101] P. Petersson, J. Olofsson, C. Brackman, H. Seyfried, J. Zetterberg, M. Richter, M. Aldén, . A. Linne, R. K. Cheng, A. Nauert, D. Geyer, and A. Dreizler, *Simultaneous PIV/OH-PLIF, rayleigh thermometry/OH-PLIF and stereo PIV measurements in a low-swirl flame*, Appl. Opt. **46** (2007), no. 19, 3928–3936.

[102] Z. Alwahabi, J. Zetterberg, and Z. et al. Li, *High resolution polarization spectroscopy and laser induced fluorescence of* CO_2 *around* $2\mu m$, Eur. Phys. J. D **42** (2007), 4147.

[103] N. Argaman and G. Makov, *Density functional theory: An introduction*, Am. J. Phys. **68** (2000), no. 1, 69–79.

[104] R. M. Dreizler and E. K. U. Gross, *Density functional theory: An approach to the quantum many-body problem*, Springer, 1990.